A diffusion model-free framework with echo time dependence for free-water elimination and brain tissue microstructure characterization

Miguel Molina-Romero[1,2,*] Pedro A. Gómez[1,2] Jonathan I. Sperl[2] Michael Czisch[3] Philipp G. Sämann[3] Derek K. Jones[4,5] Marion I. Menzel[2] Bjoern H. Menze[1]

1 Computer Science, Technical University Munich, Munich, Germany

2 GE Global Research Europe, Garching, Germany

3 Max Planck Institute of Psychiatry, Munich, Germany

4 CUBRIC, Cardiff University, Cardiff, UK

5 School of Psychology, Faculty of Health Sciences, Australian Catholic University, Victoria, Australia

***** Corresponding author:

Name	Miguel Molina Romero
Department	Computer Science
Institute	Technical University Munich
Address	Boltzmannstr 11
	85748 Garching
	Germany
E-mail	miguel.molina@tum.de

Manuscript word count: 5000

Abstract word count: 200

Abstract

Purpose: The compartmental nature of brain tissue microstructure is typically studied by diffusion MRI, MR relaxometry or their correlation. Diffusion MRI relies on signal representations or biophysical models, while MR relaxometry and correlation studies are based on regularized inverse Laplace transforms (ILTs). Here we introduce a general framework for characterizing microstructure that does not depend on diffusion modeling and replaces ill-posed ILTs with blind source separation (BSS). This framework yields proton density, relaxation times, volume fractions and signal disentanglement, allowing for separation of the free-water component.

Theory and Methods: Diffusion experiments repeated for several different echo times, contain entangled diffusion and relaxation compartmental information. These can be disentangled by BSS using a physically constrained non-negative matrix factorization.

Results: Computer simulations, phantom studies, together with repeatability and reproducibility experiments demonstrated that BSS is capable of estimating proton density, compartmental volume fractions and transversal relaxations. In vivo results proved its potential to correct for free-water contamination and to estimate tissue parameters.

Conclusion: Formulation of the diffusion-relaxation dependence as a BSS problem introduces a new framework for studying microstructure compartmentalization, and a novel tool for free water elimination.

Keywords: brain microstructure, diffusion MRI, blind source separation, free-water elimination, MR relaxometry, non-negative matrix factorization

Introduction

More than fifty years have passed since Stejskal and Tanner published their early research on pulsed gradient spin-echo (PGSE) (1). Thereafter, diffusion weighted imaging (DWI) became an essential tool for non-destructive tissue microstructure characterization. The pioneering studies on ex vivo tissue and simulations of Krägger (2), Latour et al. (3), Szafer et al. (4), and Stanisz et al.(5) established the theoretical basis of the compartmental model of neural tissue.

These early contributions were later translated to target specific biomarkers for in vivo human studies. White matter (WM) anisotropy became fiber orientation with the introduction of diffusion tensor imaging (DTI) (6). The composite hindered and restricted model of diffusion MR imaging (CHARMED) (7) extended DTI to two compartments with restricted and hindered diffusion behavior. Using the same principles, the neurite orientation dispersion and density imaging (NODDI) model (8) introduced fiber orientation dispersion metrics and added an isotropic compartment. Additionally, axon diameter was addressed by AxCaliber (9) and ActiveAx (10). These and other approaches rely on diffusion signal representations or a variety of geometric biophysical assumptions about the underlying tissue compartments, producing a wide range of possible configurations (11).

In parallel with the development of multicomponent diffusion tissue models, relaxometry addressed the compartmental nature of tissue microstructure from a different perspective (12). Multi-echo spin echo (SE) experiments combined with regularized inverse Laplace transforms (ILTs) for multi-exponential fitting showed the presence of multiple water compartments in the tissue. Non-negative least squares (NNLS) (13) is the current gold standard for computing a regularized discrete ILTs for several components (14, 15). Alternatively, the exponential analysis via system identification using Steiglitz–McBride (EASI-SM) for multicomponent estimation was introduced by Stoika et al. (16, 17). Additionally, mcDESPOT (18), used a spoiled gradient-recalled echo and a balanced steady-state free precession to yield relaxation, volume fraction, and water exchange parameters for three compartments.

Nevertheless, the paths of diffusion MRI and MR relaxometry have become entangled over the years. Studies on ex vivo nerves with a diffusion-weighted Carr-Purcell-Meiboom-Gill (CPMG) sequence (19, 20) showed the relationship that existed between compartmental T_2 decay and diffusivity. However, diffusion-weighted CPMG experiments need long acquisition times and high specific absorption rates, which makes them unsuitable for human in vivo studies. Typically, two-dimensional ILTs were used to fit the data, but this approach is highly ill-posed and requires large

amounts of data for stabilization. Recently, Benjamini et al. (21) introduced the marginal distributions constrained optimization (MADCO), a non-CPMG compressed-sensing based solution that reduced the amount of data necessary for NMR diffusion-relaxation correlation experiments. Kim et al. translated diffusion-relaxation correlation spectroscopy (DR-COSY) (22, 23) into imaging (DR-CSI) (24) using spatial regularization to reduce the amount of necessary data and stabilize the ILTs. However, they require specific diffusion protocols with increasing b-values along a unique diffusion direction and repeated echoes or inversion times. Other alternatives combine diffusion models with multicompartmental relaxation. For instance, inversion recovery DWI has been used to identify fiber populations (25, 26), and WM integrity has been characterized using the axonal stick model and multiple echo times (TE) (27).

Compartmental analysis of the diffusion signal is intimately related to a recurring issue: cerebrospinal fluid (CSF) contamination (28, 29). All the existing contributions agree on using a bi-tensor signal model: parenchyma and CSF. However, this is an ill-posed problem for a single-shell and ill-conditioned for multiple-shell acquisitions (30). Spatial regularization was proposed by Pasternak et al. (31), relying on the local smoothness of the diffusion tensor. Later, a protocol optimization for multiple shells was presented by Hoy et al. (32), eliminating such a constraint. Other solutions regularize the problem by adding priors (33) or finding the best fit to the model (34). Nevertheless, the CSF contribution to the diffusion signal depends on the TE. Thus, disentangling the tissue CSF volume fraction requires an approach that includes T_2 compartmental dependencies (33, 35, 36).

We propose a general framework for studying diffusion and relaxation characteristics in tissue microstructures. We call it general because it does not model the compartmental diffusion behavior. It replaces the ILTs by a blind source separation (BSS) technique, reducing the minimum number of distinct echo times required to the number of compartments in the tissue, less than for ILTs-based methods. Other than the requirement to measure at more than one echo time, this framework is diffusion protocol-agnostic, and can be used in combination with any protocol of interest. Our approach quantifies proton density (PD), compartmental volume fractions, and transverse relaxation times. Importantly, it handles diffusion signals from each compartment independently, allowing for individual analyses, and thus performs CSF partial volume correction as a direct application.

Theory

Following the Bloch-Torrey equation, we describe the diffusion signal as a weighted sum of the signals from the compartments comprising the tissue:

$$X(TE, b, \mathbf{g}) = S_0 \sum_{i=1}^{M} f_i e^{-\frac{TE}{T_{2_i}}} S_i(b, \mathbf{g}). \quad [1]$$

Where b summarizes the gradient effects (1, 37) and $\mathbf{g}$ defines the gradient directions. Here, the compartmental diffusion sources $S_i(b, \mathbf{g})$ are weighted by their volume fraction, f_i, TE and T_{2_i}. The exponent (the ratio between TE and T_{2_i}) scales the contribution of each compartment to the acquired signal. Therefore, measuring at different TEs produces distinct diffusion signals (38) with different weights from the compartmental signal sources.

As a result, the signal of a single voxel measured with a protocol that accounts for multiple echoes can be formulated as:

$$\begin{bmatrix} X_1(TE_1, b, \mathbf{g}) \\ \vdots \\ X_N(TE_N, b, \mathbf{g}) \end{bmatrix} = S_0 \begin{bmatrix} f_1 e^{\frac{-TE_1}{T_{2_1}}} & \cdots & f_M e^{\frac{-TE_1}{T_{2_M}}} \\ \vdots & \ddots & \vdots \\ f_1 e^{\frac{-TE_N}{T_{2_1}}} & \cdots & f_M e^{\frac{-TE_N}{T_{2_M}}} \end{bmatrix} \begin{bmatrix} S_1(b, \mathbf{g}) \\ \vdots \\ S_M(b, \mathbf{g}) \end{bmatrix}, \quad [2]$$

where X_j ($j \in [1, N]$) are the diffusion signals acquired for the N TEs. f_i and T_{2_i} ($i \in [1, M]$) are the volume fraction and T_2 decay for the ith compartment, respectively, and M is the number of compartments.

Equation 2 can be expressed in matrix form as $\mathbf{X}$=$\mathbf{AS}$. This is a matrix factorization of the measurements, $\mathbf{X} \in \mathbb{R}_{\geq 0}^{N \times n}$, into two new matrices: the mixing matrix, $\mathbf{A} \in \mathbb{R}_{\geq 0}^{N \times M}$, which is defined by the experimental TEs, the compartmental volume fractions f, and T_2 decays; and the sources matrix, $\mathbf{S} \in \mathbb{R}_{\geq 0}^{M \times n}$, representing the diffusion sources in each sub-voxel compartment. Interestingly, we noticed from the definition of $\mathbf{A}$ that the ratio between the experimental TEs and T_{2_i} determines the direction (or slope for $N = 2$) of the ith column vector of the mixing matrix. Therefore:

$$T_{2_i} = \frac{TE_k - TE_l}{log(\frac{a_{li}}{a_{ki}})}, \quad [3]$$

where $TE_k < TE_l$, and a_{ki} and a_{li} are the kth and lth elements of the ith column of the mixing matrix, respectively.

Additionally, diffusion is an attenuation contrast and as such, $S(b=0)=1$, allowing Eq. 2 to be rewritten as

$$\begin{bmatrix} X_1(TE_1, b=0, \mathbf{g}) \\ \vdots \\ X_N(TE_N, b=0, \mathbf{g}) \end{bmatrix} = S_0 \begin{bmatrix} e^{\frac{-TE_1}{T_{2_1}}} & \cdots & e^{\frac{-TE_1}{T_{2_M}}} \\ \vdots & \ddots & \vdots \\ e^{\frac{-TE_N}{T_{2_1}}} & \cdots & e^{\frac{-TE_N}{T_{2_M}}} \end{bmatrix} \begin{bmatrix} f_1 \\ \vdots \\ f_M \end{bmatrix}, \quad [4]$$

which, together with $\sum_{i=1}^{M} f_i = 1$, allows us to solve for the volume fractions and proton density (f_i and S_0) when the number of measurements matches the number of compartments ($M = N$). Contrary, when there are more compartments than measurements ($M > N$), Eq. 4 is undetermined and f_i and S_0 cannot be estimated.

Factorizing $\mathbf{X}$ into $\mathbf{A}$ and $\mathbf{S}$ is known as blind source separation (BSS) (39) of mixed measurements into their generating sources (Figure 1). For BSS to identify these sources, they have to be distinct: $S_i \neq S_j \; \forall \; i \neq j$. Therefore, based on previous work (19, 20), we assumed them to be different.

There are four main approaches to BSS: principal component analysis (PCA) (40), independent component analysis (ICA) (41), non-negative matrix factorization (NMF) (42) and sparse component analysis (SCA) (43). PCA is not an applicable solution for this problem because the diffusion sources are not orthogonal. ICA assumes, as prior knowledge, that the signal sources are statistically independent and have non-Gaussian distributions. However, diffusion MRI signals are correlated with the tissue structure and temperature and they present non-Gaussian distributions only in restricted compartments, meaning that ICA is not suitable either. We previously explored SCA (44) and found that even though the results for simulations and real data for specific diffusion protocols were encouraging, finding a sparse and disjoint domain to meet the method's requirements was not always possible for arbitrary protocols. We observed the same issue for a version of NMF that enforces sparsity similarly (36).

In the present work, we took a BSS approach based on NMF (assuming $\mathbf{X}$, $\mathbf{A}$, and $\mathbf{S}$ are non-negative). Instead of depending on sparsity, we used a popular NMF solver: the alternating least squares algorithm (ALS) (42, 45, 46). We chose ALS instead of the multiplicative update algorithm (47) due to its faster convergence (48). We extended ALS to account for physically plausible limitations, resulting in Algorithm 1, which we refer to as constrained alternating least squares (cALS). Compartmental T_2 values available from the literature (15) allowed us to limit the solution space of the columns of $\mathbf{A}$ (Eq. 3). Additionally, for in vivo data, the diffusion behavior

of CSF is known to be approximately isotropic with 3×10^{-3} mm^2/s diffusivity (28), adding extra prior information. These constraints and priors make cALS converge toward physically realistic solutions (Figure 1).

Algorithm 1 Constrained Alternating Least Squares (cALS)

procedure cALS($\mathbf{X}$)
  Use priors on T_2 and experimental TEs to initialize the direction of the columns of $\mathbf{A}$ at the central T_2 value of the solution space of each column.
  while iter $<$ maximum iterations **do**
    Solve for $\mathbf{S}$ in $\mathbf{A}^T\mathbf{AS}=\mathbf{A}^T\mathbf{X}$. ▷ Least Squares.
    Set all negative elements of $\mathbf{S}$ to 0. ▷ Non-negativity.
    [Fix the one element of $\mathbf{S}$ to a known signal.] ▷ If analytical expression is known.
    Solve for $\mathbf{A}$ in $\mathbf{SS}^T\mathbf{A}^T=\mathbf{SX}^T$. ▷ Least Squares.
    Set all negative elements of $\mathbf{A}$ to 0. ▷ Non-negativity.
    Constrain the directions of the columns of $\mathbf{A}$. ▷ T_2 consistency.
    $error_i = \|A - SX\|^2$
    if $error_i < tolerance$ **then**
      break ▷ Check for data consistency.
    end if
    if $error_i >= error_{i-1}$ **then**
      break ▷ Check for convergence.
    end if
  end while
  return $\mathbf{A}$
end procedure

Constrained ALS initializes the column vectors of $\mathbf{A}$ at the central T_2 of their given constraints, avoiding random initializations in regions that are not physically feasible and increasing the stability. After each iteration, cALS verifies that the resulting T_2 of each column vector is between its boundaries, and sets it back to the center of its constrained solution space otherwise.

Following the factorization of $\mathbf{A}$, we estimated T_2 and f for each compartment, (Eqs. 3 and 4), and recalculated the real $\mathbf{A}$. This is important since the column norms of the factorized $\mathbf{A}$ do not tell us about the volume fractions. Then, $\mathbf{S}=\mathbf{A}^{-1}\mathbf{X}$ is calculated.

An iterative algorithm like cALS inverts **A** repeatedly, requiring it to be non-singular and introducing a new condition. From Eq. 2, **A** is non-singular when $T_{2_i} \neq T_{2_j}\ \forall\ i \neq j$. Hence, in accordance with the literature (19, 20), we assumed that the transverse relaxation times for each compartment were distinct.

An open source implementation can be found in https://github.com/mmromero/dwybss.

Methods

Simulations

NMF is known for converging to local minima (45). Thus, it is necessary to asses the impact of the constraints. We ran simulations with Rician noise for signal-to-noise ratio (SNR) levels of 50, 100, and 150 at the non-diffusion weighted volume and minimum TE. We accounted for T_2 values, volume fractions, and diffusivities supported by literature (15, 28).

Two compartments

Two compartments were simulated mimicking IE and CSF water. The diffusion protocol included one non-diffusion weighted volume and 30 directions. We modeled diffusion as a Gaussian process (see Figure S4). For all the simulations we used $T_{2_{CSF}} = 2000$ ms, and varied $T_{2_{IE}}$ from 50–150 ms in 30 increments (15). Values of $f_{IE} = 0.25$, 0.5 and, 0.75 were used. We fixed $\text{TE}_1 = 60$ ms, and explored TE_2 from 70–150 ms in 31 increments. We defined $\Delta\text{TE} = \text{TE}_2$ - TE_1. The performance of the cALS algorithm was tested under the following conditions:

1. **Overlapped T_2 constraints:** $T_{2_{IE}}$ and $T_{2_{CSF}}$ were bounded from 0–1000 and 0–3000 ms respectively, and no assumption on S_{CSF} was made (Figures 2 and S5).

2. **Overlapped T_2 constraints and prior S_{CSF}:** $T_{2_{IE}}$ and $T_{2_{CSF}}$ were bounded from 0–1000 and 0–3000 ms respectively. CSF diffusivity was assumed to be isotropic with value 3×10^{-3} mm^2/s (Figure S10).

3. **Separated T_2 constraints:** $T_{2_{IE}}$ and $T_{2_{CSF}}$ were bounded from 0–300 and 300–3000 ms respectively, and no assumption on S_{CSF} was made (Figure S11).

4. **Separated T_2 and prior S_{CSF}:** $T_{2_{IE}}$ and $T_{2_{CSF}}$ were bounded from 0–300 and 300–3000 ms respectively. CSF diffusivity was assumed to be isotropic with value 3×10^{-3} mm^2/s (Figure

S13).

5. **Fixed $T_{2_{CSF}}$:** $T_{2_{IE}}$ was bounded from 0–300 ms. $T_{2_{CSF}}$ was fixed to 2000 ms. No assumption on S_{CSF} was made (Figure S12).

6. **Fixed $T_{2_{CSF}}$ and prior S_{CSF}:** $T_{2_{IE}}$ was bounded from 0–300 ms. $T_{2_{CSF}}$ was fixed to 2000 ms. CSF diffusivity was assumed to be isotropic with value 3×10^{-3} mm^2/s (Figures 3 and S6).

We repeated the last simulation for values of $f_{IE} = 0$ and 1, accounting only for IE or CSF (Figures 4 and S7).

Finally, intra-cellular (IC) and extra-cellular (EC) T_2 values are similar (15). We assessed the potential of BSS to separate them. Two diffusion signals were generated (see Figure S14). We used $f_{IC} = 0.25$, 0.5, and 0.75. The $T_{2_{IC}}$ vales ranged from 50–90 ms in 30 increments, and $T_{2_{EC}} = 100$ ms. TE_1 was fixed to 60 ms and TE_2 was varied between 70–150 ms in 31 increments. No assumption was made on the diffusion signals, and T_2 constraints were defined between 0–150 and 0–200 ms for IC and EC respectively (Figures 5 and S8).

We simulated 1000 times each combination of parameters, and reported the mean value of the absolute error of f, the relative error of T_2, and their standard errors (SEM).

Three compartments: searching for myelin

We incorporated a fast decaying component to model myelin, and fixed the T_2 of myelin (T_{2_M}) to 15 ms (15). $T_{2_{IE}}$ was varied from 50–150 ms in 30 increments, and $T_{2_{CSF}} = 2000$ ms. To account for short T2 components we needed to reduce the minimum TE of our simulations (see phantom experiments in the supporting material). Therefore, we fixed $TE_1 = 10$ ms, $TE_3 = 150$ ms, and varied TE_2 from 20–140 ms in 31 increments. We defined $\Delta TE = TE_2 - TE_1$. Three cases were explored: 1) $f_M = 0.1$, $f_{IE} = 0.6$; 2) $f_M = 0.2$, $f_{IE} = 0.5$; and 3) $f_M = 0.3$, $f_{IE} = 0.4$; keeping $f_{CSF} = 0.3$ for all of them. Simulations were run for two cases:

1. **Overlapped T_2 constraints:** T_{2_M}, $T_{2_{IE}}$, and $T_{2_{CSF}}$ were bounded from 0–40, 0–300, and 0–3000 ms respectively. No assumption on S_{CSF} was made.

2. **Separated T_2 constraints, fixed $T_{2_{CSF}}$ and prior S_{CSF}:** T_{2_M} and $T_{2_{IE}}$ were bounded from 0–40 and 41–300 ms respectively, while $T_{2_{CSF}} = 2000$ ms. CSF diffusivity was assumed to be isotropic with value 3×10^{-3} mm^2/s (Figures 6 and S9).

Each combination of parameters was simulated 1000 times. The mean value of the absolute error of f, the relative error of T_2, and their SEM were reported.

In vivo clinical data: free-water elimination

We aim to show that BSS has potential applications in clinical settings. To this end, we ran an experiment to analyze its performance for estimating tissue parameters and correcting for CSF contamination.

Data acquisition

Two volunteers, a male (age 28 years) and a female (age 24 years) were scanned in a 3.0 T GE MR750w (GE Healthcare, Milwaukee, WI). The in vivo study protocol was approved by our institutional review board and prior informed consent was obtained. We acquired seven diffusion PGSE echo planar imaging (EPI) volumes for TE values from 75.1–135.1 ms in 10 ms increments. The following parameters were constant: FOV = 240 mm; 4 mm slice thickness; TR = 6000 ms; 96×96 matrix size; ASSET = 2; and 30 directions. Additionally, we measured fluid-attenuated inversion recovery (FLAIR) SE EPIs for 17 equally-spaced TEs ranging from 20–260 ms. The same imaging parameters were used as for the diffusion experiments but with no acceleration (ASSET = 0).

Data analysis

Diffusion data for all TEs were first registered with FSL FLIRT (49) to the shortest TE volume. We then processed them with BSS in pairs ($M = N = 2$) with a fixed short TE of 75.1 ms. The long TE was increased from 85.1 to 135.1 ms for a total ΔTE of 60 ms (Figures 7 and 8). We used literature CSF values ($T_{2_{CSF}} = 2$ s and $D_{CSF} = 3 \cdot 10^{-3}$ mm^2/s) as the prior knowledge, and constrained the possible values of $T_{2_{IE}}$ between 0–200 ms (15, 28). We report maps of the BSS relative factorization error (Figure 7a, 7b and 7g), CSF volume fraction (Figure 7c and 7h), proton density (Figure 7d and 7i), $T_{2_{IE}}$ (Figure 7e and 7j) and number of compartments (Figure 7f and 7k).

For reference, FLAIR multi-echo EPI data were also registered with FLIRT to the shortest TE non-diffusion weighted volume. The signal decay for each voxel was then matched to a dictionary of mono-exponential decays from 0–300 ms with a grid of 1 ms. We compared this map against the BSS $T_{2_{IE}}$ map (Figure 8).

We defined the relative error of the matrix factorization for the in vivo data as follows:

$$\epsilon = \frac{|\mathbf{X} - S_0\mathbf{AS}|_2}{|\mathbf{X}|_2}. \quad [5]$$

This is a measure of the performance of BSS for each voxel. Given that we calculated $\mathbf{S}=\mathbf{A}^{-1}\mathbf{X}$, this error formulation is sensitive to: 1) breaches of the BSS conditions due to artifacts, and 2) numerical instabilities due to the condition of $\mathbf{A}$. Point one is the result of B_0 drift, subject motion, flow, and eddy currents. These effects produce a violation of the BSS condition, making the signal sources different between TE measurements. The second point is the error amplification factor. A high ϵ denotes that the factorization could not find a solution within the constrained space and thus, results might not be trustworthy.

Finally, BSS does not model the compartmental diffusion signal. However, to demonstrate a simple way to perform compartment-independent analysis and correct for CSF contamination, we fitted the measured and disentangled signals to the DTI model (6). We fitted the measured diffusion volumes at the shortest TE, and the BSS separated signals for the IE and CSF compartments to a mono-exponential model using standard linear regression (FSL FDT Toolbox (http://www.fmrib.ox.ac.uk/fsl)). For comparison, bi-exponential models using Pasternak's and Collier's methods were used (Figures 9, S15 and 10). Fractional anisotropy (FA) and mean diffusivity (MD) maps were derived for each fit.

Results

Simulations

Two Compartments

The convergence area is the region where the mean relative error of $T_{2_{IE}}$ is lower than 0.1 per unit (p.u). Its shape for all the simulations (Figures 2, 3, 4, 5, S5, S6, S7, S8, S10, S11, S12, and S13) follows two effects. First, the condition number of the mixing matrix limits the lower bound of ΔTE – similar TE values produce more linearly dependent column vectors of $\mathbf{A}$ –. And second, the SNR plays a double role, it increases the error regions where $\mathbf{A}$ is bad-conditioned (small ΔTE), and limits the maximum ΔTE due to the T_2 decay of the signals. Thus, when the SNR increases the convergence area grows and the region of minimum SEM, denoting an improvement on the stability of the algorithm. The convergence area also depends on the IE volume fraction. The larger is the

contribution of IE, the better is th $T_{2_{IE}}$ estimate.

Adding priors on S_{CSF} improves the $T_{2_{IE}}$ estimate, even at SNR = 50 (Figure S10). Bounding the solution space into non-overlapping regions also improves the results of $T_{2_{IE}}$ (Figure S11), although less than combining it with CSF prior knowledge (Figure S13). The $T_{2_{CSF}}$ estimate shows a 0.17 p.u. due to the small variation of S_{CSF} along the acquired TEs (4.4 %). This is corrected when relaxometry prior is incorporated (Figures 3 and S12). The comparison between Figure 2 and 3, show the benefit of including prior knowledge into the factorization algorithm, specially at low SNR. Then, the accuracy of the estimates will be influenced by the selection of ΔTE, the T_2 boundaries, the S_{CSF} prior, and the expected $T_{2_{IE}}$ and f_{IE} values. We used literature values for $T_{2_{IE}}$, $T_{2_{CSF}}$ (15), and S_{CSF} (28). According to Figures 3a and 3b one needs a minimum ΔTE of 26 ms for an accurate f_{IE} estimate. Interestingly, f_{IE} is a reliable parameter that tell us about the bias of $T_{2_{IE}}$, the larger f_{IE} is, the more accurate $T_{2_{IE}}$ becomes (3a and 3c).

For one tissue compartment BSS is able to precisely (SEM < 0.01) estimate the volume fraction with mean absolute error below 0.1 when ΔTE > 35 ms (Figure 4a and 4b). When $f_{IE} = 1$ the area of mean convergence of the $T_{2_{IE}}$ estimate is almost independent from ΔTE (4c and 4d). We found an equivalent result for the mean relative error of $T_{2_{CSF}}$ when $f_{IE} = 0$ (4e and 4f), although in this case it comes from the $T_{2_{CSF}}$ prior. Notice the large error and instability of $T_{2_{IE}}$ and $T_{2_{CSF}}$ in the opposite cases, $f_{IE} = 0$ and $f_{IE} = 1$ respectively (Figures 4c and 4e). This results when BSS tries to find a component that is not in the tissue and thus, cannot be estimated.

For two components with similar T_2 values and little priors (IC and EC) cALS losses efficiency. The volume fraction estimates are biased (Figure 5a), and $T_{2_{IC}}$ shows a narrow convergence region that is almost independent of ΔTE. The lower bound of this region is limited by the proximity of $T_{2_{IC}}$ and $T_{2_{EC}}$ that worses the condition of $\mathbf{A}$. The upper bound results of the lack of prior on the signal of one of the compartments, in contrast with the S_{CSF} prior used before (compare Figures 2 and S10) that increased the convergence area towards lower T_2 values.

Three Compartments: searching for myelin

The convergence area is the one where the errors of f_M, f_{IE}, T_{2_M}, and $T_{2_{IE}}$ are lower than 0.1 in absolute value for the volume fractions and per unit for T_2. Figures 6a, 6c, 6e, and 6g show and optimal ΔTE = 36 ms. Notice that when ΔTE increases the error of the myelin parameters grows due to the reduction of the myelin contribution to the second TE, worsening the SNR of that component (Figures 6a and 6e). Since all the volume fractions add up to one, errors on f_M increase

the error on f_{IE} (Figures 6a and 6c). The estimate of $T_{2_{IE}}$ is dependent on SNR and its volume fraction, compounding its calculation for SNR < 50 and $f_{IE} < 0.4$ (Figure S9g lower left corner).

One should notice that including a third compartment increases the condition number of $\mathbf{A}$, rising the instability of the factorization (Figure 6f). See the phantom experiments in the supporting material.

In vivo clinical data: free-water elimination

We observed that the mean relative error for the whole brain ($\langle\epsilon\rangle$) decreased as ΔTE increased (Figures 7a, 7b, and 7g), in agreement with phantom findings (see supporting material) and the results of the simulations for two compartments. Interestingly, for the maximum ΔTE, we can see that the number of compartments is two in regions next to the ventricles and the cortex, but one inside the ventricles and in some deep WM areas (Figure 7k). It is also noteworthy that the pure CSF areas (e.g., the ventricles) have been removed from the $T_{2_{IE}}$ map (Figures 7e and 7j), while the opposite is observed in the CSF volume fraction (Figures 7c and 7h), indicating a successful disentangling effect.

We compared the BSS-estimated $T_{2_{IE}}$ maps for increasing ΔTE values with the reference map obtained from the FLAIR multi-echo SE data. We noted how the structural similarity index (50) increased and the mean relative error decreased as ΔTE grew (Figure 8a and 8b). Additionally, the histograms for both subjects tended toward the reference as the difference between the short and long TEs grew. This reflects an underestimation of $T_{2_{IE}}$ for small ΔTE values that can be explained by Eq. 3 and Figure S1c. Moreover, the FLAIR T_2 map showed high values in the ventricles, possibly indicating imperfect CSF suppression and, thus, slightly increased reference values (Figure 8a, 8c, and 8d).

FA and MD maps and histograms were calculated from the BSS IE and CSF disentangled signals for both subjects (Figures 9, S15, and 10). These maps displayed an overestimation of the CSF volume fraction for low ΔTE values (the low FA peak in Figures 9b and S15b was removed). This resulted in a compensation effect for the previously shown underestimation of $T_{2_{IE}}$. Additionally, the FA histograms (Figures 9b and S15b) showed a tendency toward higher FA values and a reduction of the low FA peak associated with free water. At long ΔTE values, FA seems to tend toward a stable distribution. We also observed an enlargement of the corpus callosum and a general recovery of peripheral WM tracts and the fornix in the colored FA maps (Figures 9a and S15a).

Additionally, on the MD histograms for IE water (Figures 9d and S15d) we found a reduced

number of voxels with diffusivities greater than 1×10^{-3} mm^2/s. In contrast, the main peak at 0.7×10^{-3} mm^2/s, associated with the parenchyma, remained in its original position, indicating that IE water represents a non-CSF tissue. This MD reduction was also visible in the maps (Figure 9c and S15c). Finally, the MD histograms for CSF water (Figure 10) showed a tendency toward 3×10^{-3} mm^2/s as ΔTE increased, in agreement with the literature (28). All these findings agreed with a disentangling of IE and CSF signals and thus, a correction of the free water partial volume effect in the diffusion signal.

Discussion

Stability

Four main approaches exist for the BSS problem (ICA, PCA, NMF, and SCA). Choosing the appropriate method depends on the prior knowledge of the signal sources. In our experiments, we relied on NMF, using a constrained version of the ALS algorithm (cALS). Others explored these algorithms before. Pauca et al. (51) used low-rank and sparsity constraints to distinguish semantic features in text mining, and later (52) smoothness regularization to identify space objects from spectral data. Gao and Church (53) also employed sparseness for cancer class discovery through gene clustering, which was later extended by Kim and Park (54) improving the balance between accuracy and sparseness through regularization. They also introduced a variation based on the active set method (55) and low-rank approximation (56). Liu et al. (57) incorporated label information to create a semi-supervised matrix decomposition method. Sun and Févotte (58) introduced a version based on the alternating direction method of multipliers (59) (ADMM), that was further stabilized by Zhang et al. (60).

Supported by previous work, we presented a biophysical inspired solution to constrain the diffusion-relaxometry NMF compartmental problem. Essentially, our cALS algorithm imposes two constraints: 1) the rows of $\mathbf{A}$ must follow exponential relationships (relaxometry); and 2) when the analytical expression of one component is known (i.e. CSF) the corresponding row in $\mathbf{S}$ is fixed (diffusion). The stability of cALS is linked to the condition of $\mathbf{A}$ and SNR; an ill-conditioned mixing matrix will lead to error propagation due to numerical instability. We optimized the experimental TEs to reduce the condition number of $\mathbf{A}$ for literature values of T_2. However, further research based on ADMM might yield better results.

We ran extensive simulations for two compartments at clinical TE values with different priors,

and three compartments at lower TEs. These simulations highlighted the importance of choosing literature supported priors to improve the convergence, especially at low SNR. Constrained ALS converges when the number of compartments in tissue is equal or lower than the expected, but it looses performance for species with similar T_2.

Phantom experiments (see supporting material) agreed with simulation results, validating that BSS was able to accurately estimate T_2 for one compartment and separate diffusion signal sources and estimate T_2 and f for two compartments. However, they also showed that scaling the cALS algorithm to three compartments, including fast T_2 decaying species, is unstable in the range of the clinically available TE values.

Finally, repeatability and reproducibility analyses (see supporting material) show that cALS yield consistent results across repetitions and subjects, highlighting its stability.

Relaxation time and volume fraction estimates

BSS provides the means to estimate T_2 relaxation values and volume fractions. Interestingly, only a number of TE repetitions equal to the number of compartments that are assumed to be in the tissue is necessary. This results of the substitution of the ILTs by BSS, in comparison to other techniques (15, 17, 21, 24). We found a good agreement between the $T_{2_{IE}}$ estimates of the FLAIR multi-echo SE for 17 TEs and those of BSS for 2 TEs. In this sense, all the measurements along the diffusion space are considered for both TEs, incorporating redundancy and reinforcing the estimation of T_2. The SNR for the in vivo data were 147 and 104 for subjects one and two. According to the simulations at $\Delta\text{TE} = 60$ ms, the expected absolute error for the volume fraction estimate is below 0.03, meaning that $T_{2_{IE}}$ is highly reliable in white matter areas, and lesser in the CSF borders.

Myelin detection

Simulations proved that our method has the potential to disentangle three compartments by reducing the minimum TE in diffusion experiments. As a result, myelin water could be incorporated into the model (Figure 6). However, we are prevented from conducting such experiments by gradient performance on clinical scanners.

Disentangling the diffusion sources and free water elimination

Unlike other multicompartment diffusion models (2, 7, 8, 11) or more recent contributions (27, 35), our approach does not model compartmental diffusion. Our framework instead relies on three

assumptions: 1) microstructural water compartments have distinct T_2 relaxation times (14, 15); 2) each have different diffusion characteristics (19, 20); and 3) the effects of the water exchange are negligible on the timescale of our experiments (9, 61). Furthermore, our solution is diffusion protocol-agnostic (only two TEs and one non-diffusion weighted volume are necessary), allowing for flexibility in the design of the acquisition protocol, which might include any number of diffusion directions and b-values. This gives it an advantage over diffusion-relaxation correlation techniques based on regularized inverse Laplace transforms (21, 24).

A promising application of the protocol-agnostics nature of our framework is correcting for free water contamination. Recently Collier et al. (35) included TE dependence in their bi-exponential diffusion tensor model to regularize the fitting problem. However, they fitted the bi-exponential DTI model directly. Contrary, our solution does not assume any particular diffusion model, we instead separated the signal from each compartment, allowing more flexible and independent study. In this regard, analysis of the signal associated with the CSF compartment can be seen as a disentanglement quality assurance metric (Figures 9, S15, and 10), or in brain tissue applications, a general indicator of the goodness-of-fit for IE and CSF.

We fitted our data to Collier's model (35) without reaching convergence, which resulted due to our single-shelled dataset. Comparison of BSS with Pasternak's free-water elimination (FWE) method (31) is show in Figures 9 and S15. We observed a good agreement between BSS for ΔTE = 60 ms and Pasternak's FWE for FAs between 0–0.2 and 0.8–1. In the middle FA range both methods disagree, BSS shows an homogeneous correction, while Pasternak's results follow the standard DTI fit from 0.2 to 0.4 and shows a correcting effect from 0.4 to 1 (Figures 9a, 9b, S15a, and S15b). It is impossible to determine which method is better (no ground-truth). However, there are two indicators that BSS might be performing better: 1) the BSS FA curve runs in parallel to the standard DTI fit from 0.2 to 0.8, denoting an stable correction without favoring any FA range; and 2) Pasternak's MD is spatially over-regularized (Figures 9c, 9d, S15c, and S15d), while BSS's MD keeps its maximum at 0.7 mm^2/s, the reference for parenchyma (28).

Long ΔTE values benefit our framework, which is not surprising and agrees with the findings of Collier et al. (35). This is not only due to the relationship between $\mathbf{A}$ and T_2 (Eq. 3 and Figure S1c) but also because longer differences between TEs produce more distinct levels of mixing and thus better codification of the information from each source. That is to say, the short TE contains more information about the fast-relaxing species, while the long TE is dominated by CSF.

Conclusions

We have introduced for the first time a blind source separation framework for expressing the relationships between diffusion signals acquired at different TEs. This new approach does not rely on diffusion modeling or the inverse Laplace transform. Our results show that, with the current hardware, blind source separation allows for disentangling the diffusion signal sources generated by each sub-voxel compartment up to two compartments, making it a suitable tool for free-water elimination. Moreover, it simultaneously estimates proton density, volume fractions, relaxation times and the number of compartments in the underlying microstructure, paving the way for tissue microstructure characterization when the hardware constraints are relieved.

Acknowledgments

The authors want to thank Dr. Ofer Pasternak for his support in the comparison of the methods. This work was supported by the TUM Institute of Advanced Study, funded by the German Excellence Initiative, and the European Commission (Grant Agreement Number 605162). DKJ was supported by a New Investigator Award from the Wellcome Trust (096646/Z/11/Z).

References

[1] Stejskal EO, Tanner JE. Spin Diffusion Measurements: Spin Echoes in the Presence of a Time-Dependent Field Gradient. J. Chem. Phys. 1965. 42:288–292.

[2] Kärger J. Der Einfluss der Zweibereichdiffusion auf die Spinechodaempfung unter Beruecksichtigung der Relaxation bei Messungen mit der Methode der gepulsten Feldgradienten. Annalen der Physik. 1971. 7:107–109.

[3] Latour LL, Svoboda K, Mitra PP, Sotak CH. Time-dependent diffusion of water in a biological model system. Proc. Natl. Acad. Sci. U. S. A. 1994. 91:1229–1233.

[4] Szafer a, Zhong J, Gore JC. Theoretical model for water diffusion in tissues. Magn. Reson. Med. 1995. 33:697–712.

[5] Stanisz GJ, Szafer A, Wright GA, Henkelman RM. An Analytical Model of Restricted Diffusion in Bovine Optic Nerve. Magn. Reson. Med. 1997. 37:103–111.

[6] Basser PJ, Mattiello J, LeBihan D. MR diffusion tensor spectroscopy and imaging. Biophys. J. 1994. 66:259–267.

[7] Assaf Y, Basser P. Composite hindered and restricted model of diffusion (CHARMED) MR imaging of the human brain. Neuroimage. 2005. 27:48–58.

[8] Zhang H, Schneider T, Wheeler-Kingshott CAM, Alexander DC. NODDI: Practical in vivo neurite orientation dispersion and density imaging of the human brain. Neuroimage. 2012. 61:1000–1016.

[9] Assaf Y, Blumenfeld-Katzir T, Yovel Y, Basser PJ. AxCaliber: a method for measuring axon diameter distribution from diffusion MRI. Magn. Reson. Med. 2008:1347–1354.

[10] Alexander DC, Hubbard PL, Hall MG, Moore EA, Ptito M, Parker GJM, Dyrby TB. Orientationally invariant indices of axon diameter and density from diffusion MRI. Neuroimage. 2010. 52:1374–1389.

[11] Ferizi U, Schneider T, Panagiotaki E, Nedjati-Gilani G, Zhang H, Wheeler-Kingshott CAM, Alexander DC. A ranking of diffusion MRI compartment models with in vivo human brain data. Magn. Reson. Med. 2014. 72:1785–92.

[12] Kimmich R. NMR : Tomography, Diffusometry, Relaxometry. Springer Berlin Heidelberg. 1997.

[13] Lawson CL, Hanson RJ. Solving Least Squares Problems (Classics in Applied Mathematics). 1987.

[14] Whittall KP, Mackay AL, Graeb DA, Nugent RA, Li DKB, Paty DW. In vivo measurement of T_2 distributions and water contents in normal human brain. Magn. Reson. Med. 1997. 37:34–43.

[15] MacKay AL, Laule C, Vavasour I, Bjarnason T, Kolind S, Mädler B. Insights into brain microstructure from the T_2 distribution. Magn. Reson. Med. 2006. 24:515–25.

[16] Stoica P, Babu P. Parameter estimation of exponential signals: A system identification approach. Digit. Signal Process. 2013. 23:1565–1577.

[17] Björk M, Stoica P. New approach to phase correction in multi-echo T2 relaxometry. J. Magn. Reson. 2014. 249:100–107.

[18] Deoni SCL, Rutt BK, Arun T, Pierpaoli C, Jones DK. Gleaning multicomponent T_1 and T_2 information from steady-state imaging data. Magn. Reson. Med. 2008. 60:1372–1387.

[19] Peled S, Cory DG, Raymond SA, Kirschner DA, Jolesz FA. Water diffusion, T_2, and compartmentation in frog sciatic nerve. Magn. Reson. Med. 1999. 42:911–8.

[20] Does MD, Gore JC. Compartmental study of diffusion and relaxation measured in vivo in normal and ischemic rat brain and trigeminal nerve. Magn. Reson. Med. 2000. 43:837–44.

[21] Benjamini D, Basser PJ. Use of marginal distributions constrained optimization (MADCO) for accelerated 2D MRI relaxometry and diffusometry. J. Magn. Reson. 2016. 271:40–45.

[22] Callaghan PT, Arns CH, Galvosas P, Hunter MW, Qiao Y, Washburn KE. Recent Fourier and Laplace perspectives for multidimensional NMR in porous media. Magn. Reson. Imaging. 2007. 25:441–444.

[23] Hurlimann MD, Venkataramanan L, Flaum C. The diffusion-spin relaxation time distribution function as an experimental probe to characterize fluid mixtures in porous media. J. Chem. Phys. 2002. 117:10223–10232.

[24] Kim D, Doyle EK, Wisnowski JL, Kim JH, Haldar JP. Diffusion-Relaxation Correlation Spectroscopic Imaging: A Multidimensional Approach for Probing Microstructure. Magn. Reson. Med. 2017. doi:10.1002/mrm.26629.

[25] De Santis S, Barazany D, Jones DK, Assaf Y. Resolving relaxometry and diffusion properties within the same voxel in the presence of crossing fibres by combining inversion recovery and diffusion-weighted acquisitions. Magn. Reson. Med. 2016. 75:372–380.

[26] De Santis S, Assaf Y, Jeurissen B, Jones DK, Roebroeck A. T1 relaxometry of crossing fibres in the human brain. Neuroimage. 2016. 141:133–142.

[27] Veraart J, Fieremans E, Novikov DS. Quantifying neuronal microstructure integrity with TE dependent Diffusion Imaging (TEdDI). In: Proc. 25th Annu. Meet. ISMRM, Honolulu. 2017. p. 0836.

[28] Pierpaoli C, Jones DK. Removing CSF Contamination in Brain DT-MRIs by Using a Two-Compartment Tensor Model. In: Proc. 12th Annu. Meet. ISMRM, Kyoto. 2004. p. 1215.

[29] Metzler-Baddeley C, O'Sullivan MJ, Bells S, Pasternak O, Jones DK. How and how not to correct for CSF-contamination in diffusion MRI. Neuroimage. 2012. 59:1394–1403.

[30] Bergmann O, Westin CF, Pasternak O. Challenges in solving the two-compartment free-water diffusion MRI model. In: Proc. 24th Annu. Meet. ISMRM, Singapore. 2016. p. 0793.

[31] Pasternak O, Sochen N, Gur Y, Intrator N, Assaf Y. Free Water Elimination and Mapping from Diffusion MRI. 2009. 730:717–730.

[32] Hoy AR, Koay CG, Kecskemeti SR, Alexander AL. Optimization of a Free Water Elimination Two-Compartment Model for Diffusion Tensor Imaging. Neuroimage. 2014:323–333.

[33] Vallée E, Douaud G, Monsch AU, Gass A, Wu W, Smith SM, Jbabdi S. Modelling free water in diffusion mri. In: Proc. 23rd Annu. Meet. ISMRM, Toronto. 2015. p. 0474.

[34] Henriques RN, Bergmann Ø, Rokem A, Pasternak O, Correia MM. Exploring the potentials and limitations of improved free-water elimination DTI techniques. In: Proc. 25th Annu. Meet. ISMRM, Honolulu. 2017. p. 1787.

[35] Collier Q, Veraart J, Dekker AJD, Vanhevel F, Parizel PM, Sijbers J. Solving the free water elimination estimation problem by incorporating T_2 relaxation properties. In: Proc. 25th Annu. Meet. ISMRM, Honolulu. 2017. p. 1783.

[36] Molina-Romero M, Gómez PA, Sperl JI, Stewart AJ, Jones DK, Menzel MI, Menze BH. Theory, validation and application of blind source separation to diffusion MRI for tissue characterisation and partial volume correction. In: Proc. 25th Annu. Meet. ISMRM, Honolulu. 2017. p. 3462.

[37] Bihan DL, Breton E. Imagerie de diffusion in-vivo par résonance magnétique nucléaire. Comptes-Rendus l'Académie des Sci. 1985. 93:27–34.

[38] De Santis S, Assaf Y, Jones DK. The influence of T2 relaxation in measuring the restricted volume fraction in diffusion MRI. In: Proc. 24th Annu. Meet. ISMRM, Singapore. 2016. p. 1998.

[39] Yu X, Hu D, Jindong X. Blind source separation: theory and applications. Science Press. 2014.

[40] Jolliffe I. Principal component analysis. New York: Springer Verlag. 2002.

[41] Hyvarinen A, Oja E. Independent Component Analysis : A Tutorial. Neural Networks. 1999. 1:1–30.

[42] Paatero P, Tapper U. Positive Matrix Factorization - A Nonnegative Factor Model With Optimal Utilization of Error-Estimates of Data Values. Environmetrics. 1994. 5:111–126. doi: 10.1002/env.3170050203.

[43] Bofill P, Zibulevsky M. Underdetermined blind source separation using sparse representations. Signal Processing. 2001. 81:2353–2362.

[44] Molina-Romero M, Gómez PA, Sperl JI, Jones DK, Menzel MI, Menze BH. Tissue microstructure characterisation through relaxometry and diffusion MRI using sparse component analysis. In: Workshop on Breaking the Barriers of Diffusion MRI, Lisbon. 2016. p. 17.

[45] Berry MW, Browne M, Langville AN, Pauca VP, Plemmons RJ. Algorithms and applications for approximate nonnegative matrix factorization. Comput. Stat. Data Anal. 2007. 52:155–173.

[46] Lin CJ. Projected Gradient Methods for Nonnegative Matrix Factorization. Neural Comput. 2007. 19:2756–2779. doi:10.1162/neco.2007.19.10.2756.

[47] Lee D, Seung H. Algorithms for non-negative matrix factorization. In: Adv. Neural Inf. Process. Syst.. 1. 2001. p. 556–562. doi:10.1109/IJCNN.2008.4634046. 0408058v1.

[48] On the Convergence of Multiplicative Update Algorithms for Nonnegative Matrix Factorization. IEEE Trans. Neural Networks. 2007. 18:1589–1596. doi:10.1109/TNN.2007.895831.

[49] Jenkinson M, Smith S. A global optimisation method for robust affine registration of brain images. Med. Image Anal. 2001. 5:143–156.

[50] Wang Z, Bovik AC, Sheikh HR, Simoncelli EP. Image quality assessment: From error visibility to structural similarity. IEEE Trans. Image Process. 2004. 13:600–612.

[51] Pauca V, Shahnaz F, Berry M, Plemmons R. Text mining using non-negative matrix factorizations. In: Proc. SIAM Int. Conf. Data Min. 2004. p. 452–456.

[52] Pauca VP, Piper J, Plemmons RJ. Nonnegative matrix factorization for spectral data analysis. Linear Algebra Appl. 2006. 416:29–47. doi:10.1016/j.laa.2005.06.025.

[53] Gao Y, Church G. Improving molecular cancer class discovery through sparse non-negative matrix factorization. Bioinformatics. 2005. 21:3970–3975. doi:10.1093/bioinformatics/bti653.

[54] Kim H, Park H. Sparse non-negative matrix factorizations via alternating non-negativity-constrained least squares for microarray data analysis. Bioinformatics. 2007. 23:1495–1502. doi:10.1093/bioinformatics/btm134.

[55] Nocedal J, Wright SJ, SpringerLink (Online service). Numerical Optimization. 2006. doi:10.1007/978-0-387-40065-5. NIHMS150003.

[56] Kim H, Park H. Nonnegative Matrix Factorization Based on Alternating Nonnegativity Constrained Least Squares and Active Set Method. SIAM J. Matrix Anal. Appl. 2008. 30:713–730. doi:10.1137/07069239X.

[57] Liu H, Wu Z, Cai D, Huang TS. Constrained Nonnegative Matrix Factorization for Image Representation. IEEE Trans. Pattern Anal. Mach. Intell. 2012. 34:1299–1311. doi:10.1109/TPAMI.2011.217.

[58] Sun DL, Févotte C. Alternating direction method of multipliers for non-negative matrix factorization with the beta-divergence. IEEE Int. Conf. Acoust. Speech Signal Process. 2014:6201–6205. doi:10.1109/ICASSP.2014.6854796.

[59] Boyd S, Parikh N, E Chu BP, Eckstein J. Distributed Optimization and Statistical Learning via the Alternating Direction Method of Multipliers. Found. Trends Mach. Learn. 2011. 3:1–122. doi:10.1561/2200000016.

[60] Zhang S, Huang D, Xie L, Chng ES, Li H, Dong M. Non-negative Matrix Factorization using Stable Alternating Direction Method of Multipliers for Source Separation. Asia-Pacific Signal Inf. Process. Assoc. Annu. Summit Conf. 2015:222–228.

[61] Sakka L, Coll G, Chazal J. Anatomy and physiology of cerebrospinal fluid. Eur. Ann. Otorhinolaryngol. Head Neck Dis. 2011. 128:309–316.

[62] Laubach HJ, Jakob PM, Loevblad KO, Baird AE, Bovo MP, Edelman RR, Warach S. A phantom for diffusion-weighted imaging of acute stroke. J Magn Reson Imaging. 1998. 8:1349–1354.

[63] Andersson JL, Skare S, Ashburner J. How to correct susceptibility distortions in spin-echo echo-planar images: application to diffusion tensor imaging. Neuroimage. 2003. 20:870–888. doi:10.1016/S1053-8119(03)00336-7.

[64] Smith SM, Jenkinson M, Woolrich MW, Beckmann CF, Behrens TE, Johansen-Berg H, Bannister PR, De Luca M, Drobnjak I, Flitney DE, Niazy RK, Saunders J, Vickers J, Zhang Y, De Stefano N, Brady JM, Matthews PM. Advances in functional and structural MR image analysis and implementation as FSL. Neuroimage. 2004. 23:S208–S219. doi: 10.1016/j.neuroimage.2004.07.051.

[65] Andersson JL, Sotiropoulos SN. Non-parametric representation and prediction of single- and multi-shell diffusion-weighted MRI data using Gaussian processes. Neuroimage. 2015. 122:166–176. doi:10.1016/j.neuroimage.2015.07.067.

[66] Cook PA, Bai Y, Seunarine KK, Hall MG, Parker GJ, Alexander DC. Camino: Open-Source Diffusion-MRI Reconstruction and Processing. In: ISMRM 14th Annual Meeting & Exhibition. volume 14. 2006. p. 2759.

Figures and Tables

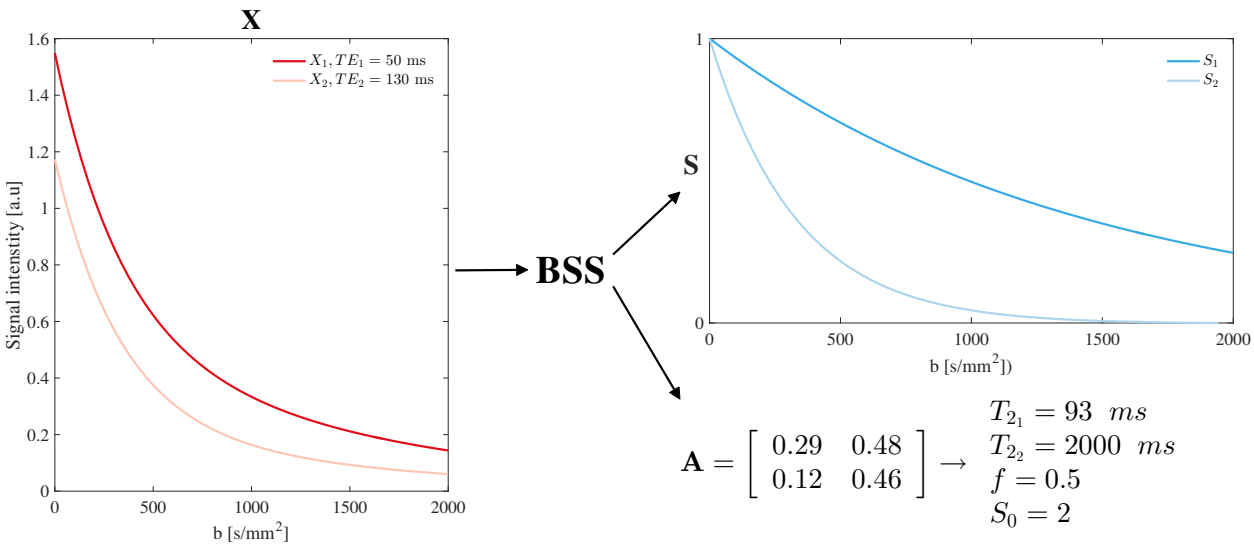

Figure 1: **Factorization of measurements, X, into the sources, S, and mixing matrix, A.** Example of a BSS operation for two mono-exponential sources ($M = 2$) and two TE measurements ($N = 2$). In this illustration, the measurements, $\mathbf{X}$, show a bi-exponential decay profile. BSS is capable of separating these two independent exponential source functions, $\mathbf{S}$; and calculating their mixing matrix, $\mathbf{A}$. The parameters that determine the degree of mixing (T_{2_1}, T_{2_2} and f), and the scaling factor, S_0, were estimated as described in Eqs. 3 and 4. We showed an exponential case for simplicity, but BSS is not limited to this choice; any signal can be processed in the same manner.

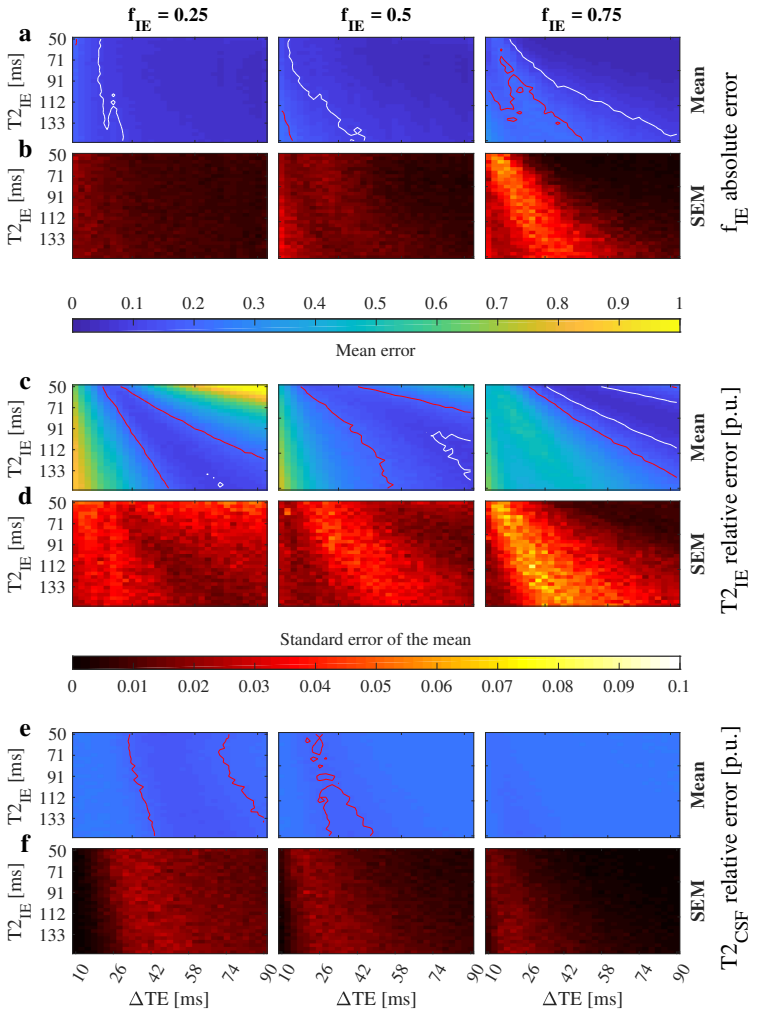

Figure 2: **Convergence for two compartments (IE and CSF) with overlapping T_2 constraints and no S_{CSF} prior (SNR = 50).**

The mean of f_{IE} absolute error and its standard error (SEM) (a and b), and the mean of $T_{2_{IE}}$ (c) and $T_{2_{CSF}}$ (e) relative errors per unit (p.u.), and their standard error (d and f).Red and white lines mark the 0.2 and 0.1 contour respectively. One thousand simulations were run for each combination of f_{IE}, $T_{2_{IE}}$, and ΔTE. $T_{2_{IE}}$ and $T_{2_{CSF}}$ were bounded between 0–1000 ms and 0–3000 ms respectively, and no prior was imposed on S_{CSF}. We defined the convergence area as the one with error lower than 0.1 for f_{IE} and $T_{2_{IE}}$. The bias of f_{IE} and $T_{2_{IE}}$ decreases for long ΔTEs as f_{IE} increases. See Figure S5 for more SNR levels.

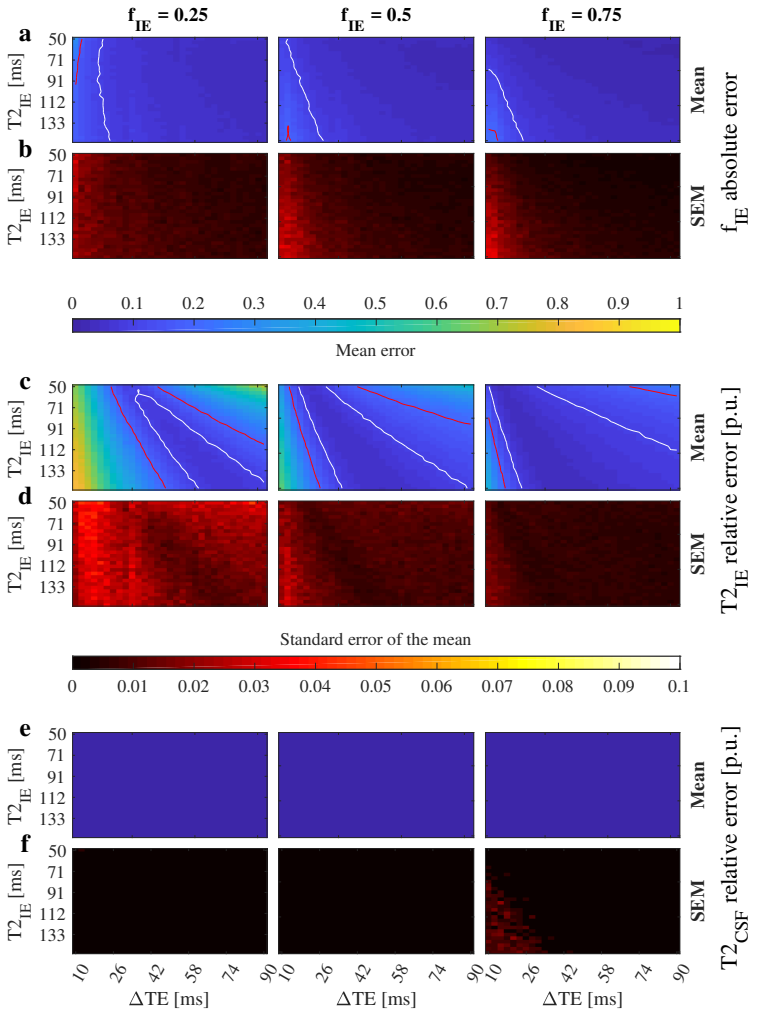

Figure 3: **Convergence for two compartments (IE and CSF) with non-overlapping T_2 constraints and S_{CSF} prior (SNR = 50).**

The mean of f_{IE} absolute error and its standard error (SEM) (a and b), and the mean of $T_{2_{IE}}$ (c) and $T_{2_{CSF}}$ (e) relative error per unit (p.u.), and their standard errors (d and f). Red and white lines mark the 0.2 and 0.1 contour respectively. One thousand simulations were run for each combination of f_{IE}, $T_{2_{IE}}$, and ΔTE. $T_{2_{IE}}$ and $T_{2_{CSF}}$ were bounded between 0–300 ms and 2000 ms respectively, and S_{CSF} was set to have isotropic diffusivity with value 3 $\times 10^{-3}$ mm^2/s. We defined the convergence area as the one with error lower than 0.1 for f_{IE} and $T_{2_{IE}}$. This area is larger than for Figure 2 stressing the importance of priors. See Figure S6 for more SNR levels.

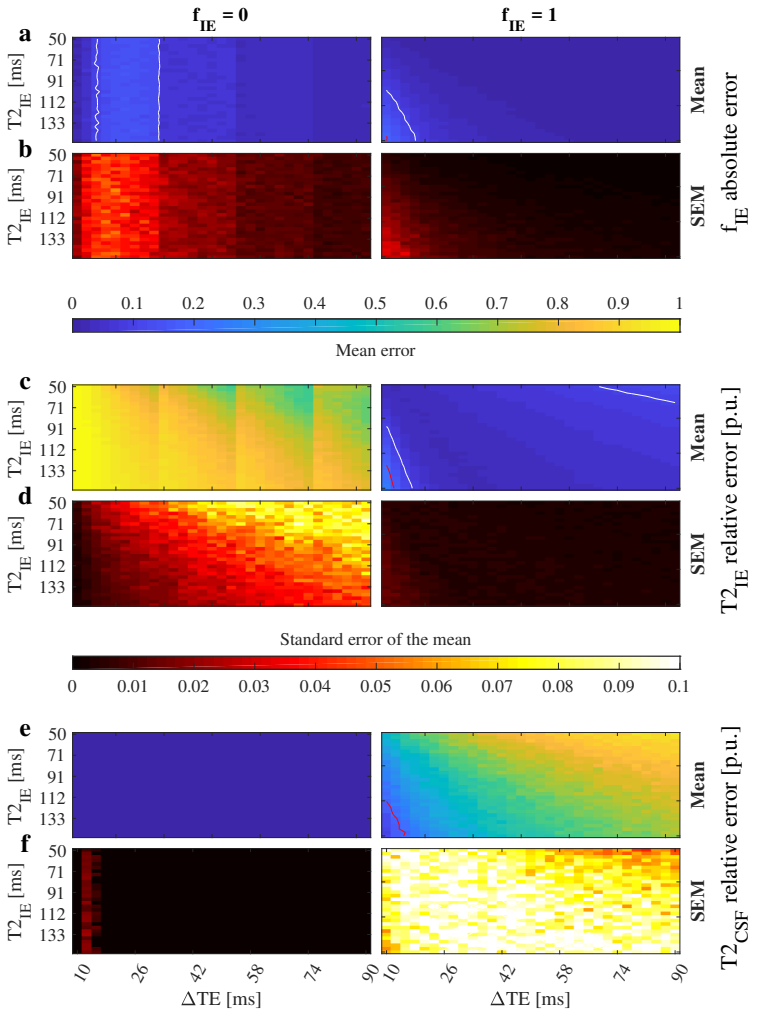

Figure 4: **Convergence for two compartments (IE and CSF) with non-overlapping T_2 constraints and S_{CSF} prior when only one is actually present in the tissue (SNR = 50).** The mean of f_{IE} absolute error and its standard error (SEM) (a and b), and the mean of $T_{2_{IE}}$ (c) and $T_{2_{CSF}}$ (e) relative error per unit (p.u.), and their standard errors (d and f). Red and white lines mark the 0.2 and 0.1 contour respectively. One thousand simulations were run for each combination of f_{IE}, $T_{2_{IE}}$, and ΔTE. $T_{2_{IE}}$ and $T_{2_{CSF}}$ were bounded between 0–300 ms and 2000 ms respectively, and S_{CSF} was set to have isotropic diffusivity with value 3 $\times 10^{-3}$ mm^2/s. We defined the convergence area as the one with error lower than 0.1 for f_{IE} and $T_{2_{IE}}$. Estimates of f_{IE} are reliable for ΔTE $>$ 45 ms (a and b). Estimates of $T_{2_{IE}}$ and $T_{2_{CSF}}$ are accurate for each case. See Figure S7 for more SNR levels.

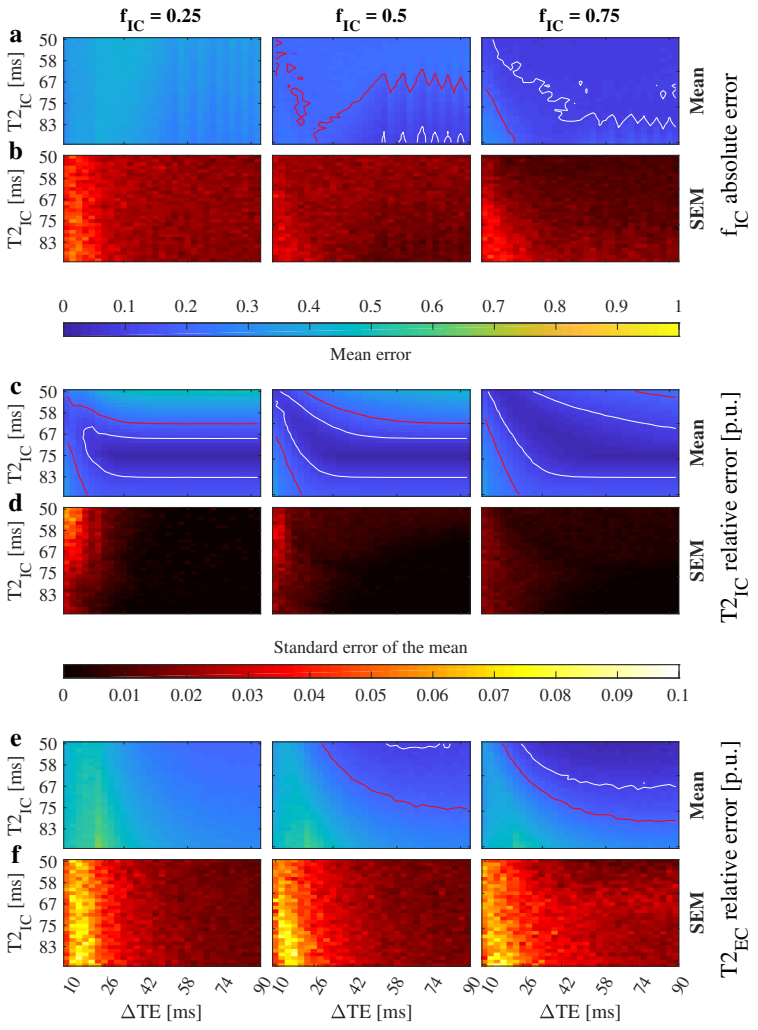

Figure 5: **Convergence for two compartments (IC and EC) with overlapping T_2 constraints and no other priors (SNR = 50).**

The mean of f_{IE} absolute error and its standard error (SEM) (a and b), and the mean of $T_{2_{IE}}$ (c) and $T_{2_{CSF}}$ (e) relative error per unit (p.u.), and their standard errors (d and f). Red and white lines mark the 0.2 and 0.1 contour respectively. One thousand simulations were run for each combination of f_{IC}, $T_{2_{IC}}$, and ΔTE. $T_{2_{IC}}$ and $T_{2_{EC}}$ were bounded between 0–150 ms and 0–200 ms respectively, and no other prior was imposed in the signal sources. We define the convergence area as the one with error lower than 0.1 for f_{IC}, $T_{2_{IC}}$, and $T_{2_{EC}}$. Estimate of f_{IC} is biased for all f_{IC} levels. T_2 estimates show a narrow band of convergence limited by the lack of prior knowledge (see Figures 2, S5 and S10) and the condition of **A** when the T_2 values are similar. See Figure S8 for more SNR levels.

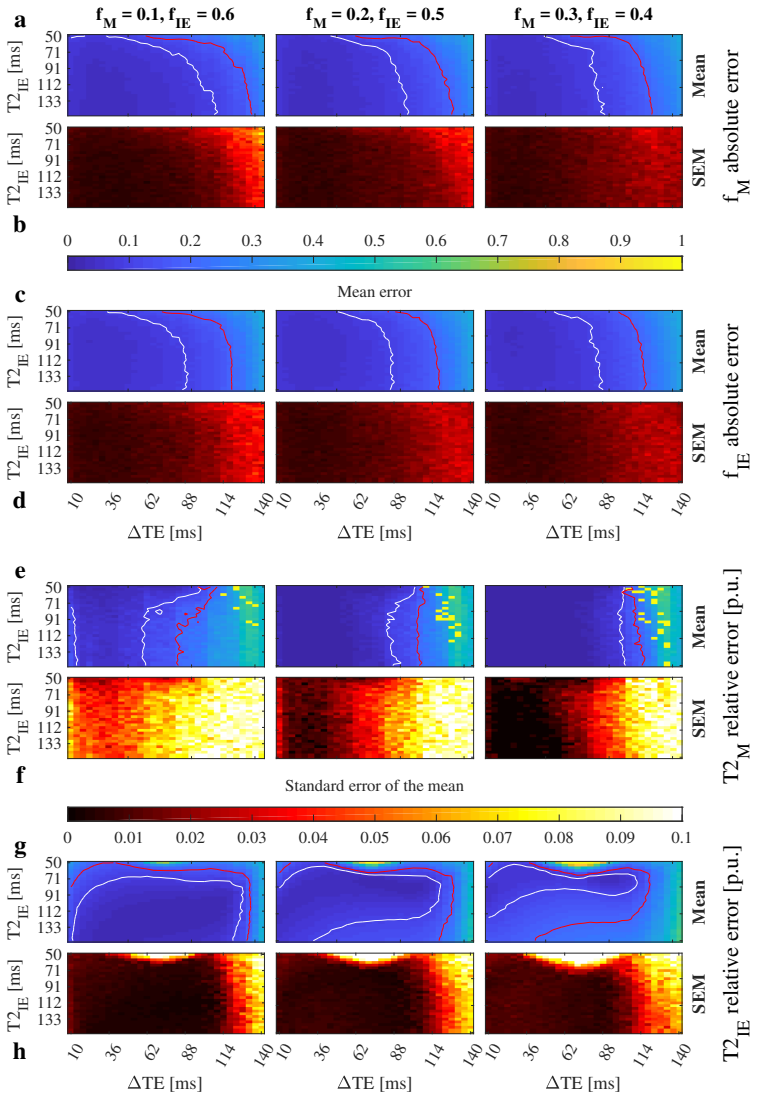

Figure 6: **Convergence for three compartments (myelin, IE, and CSF) with non-overlapping T_2 constraints and S_{CSF} prior (SNR = 50).**

The mean absolute errors of the volume fraction estimates and their standard errors (SEM) (a, b, c, and d); and the mean of T_{2_M} (e) and $T_{2_{IE}}$ (g) relative error per unit (p.u.), and their standard errors (f and h). Red and white lines mark the 0.2 and 0.1 contour respectively. There is a large convergence area when $TE_1 = 10$ ms, $TE_2 = 46$ ms, and $TE_3 = 150$ ms, which is not reachable with current clinical hardware. See Figure S9 for more SNR levels.

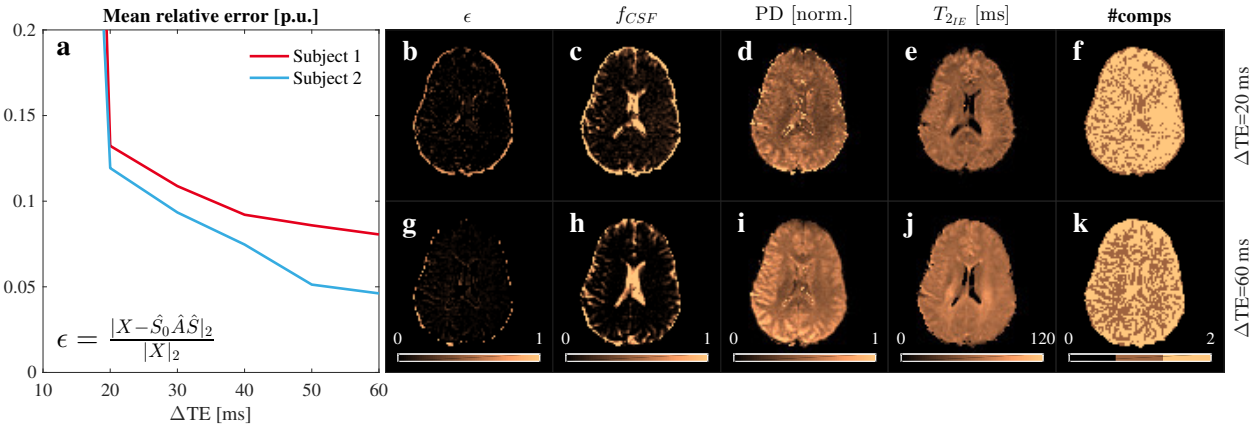

Figure 7: **BSS relative factorization error for increasing ΔTE values.**

The evolution of the relative factorization error with ΔTE, averaged over the whole brain, is shown in (a). As an example of how this error reduction affects BSS estimates we also show the relative error maps (b) and (g), CSF volume fractions (c) and (h), PDs (d) and (i), $T_{2_{IE}}$ values (e) and (j) and the number of compartments (f) and (k) for ΔTEs values of 20 and 60 ms. The mean relative factorization error decreases as ΔTE increases, improving the parameter estimates.

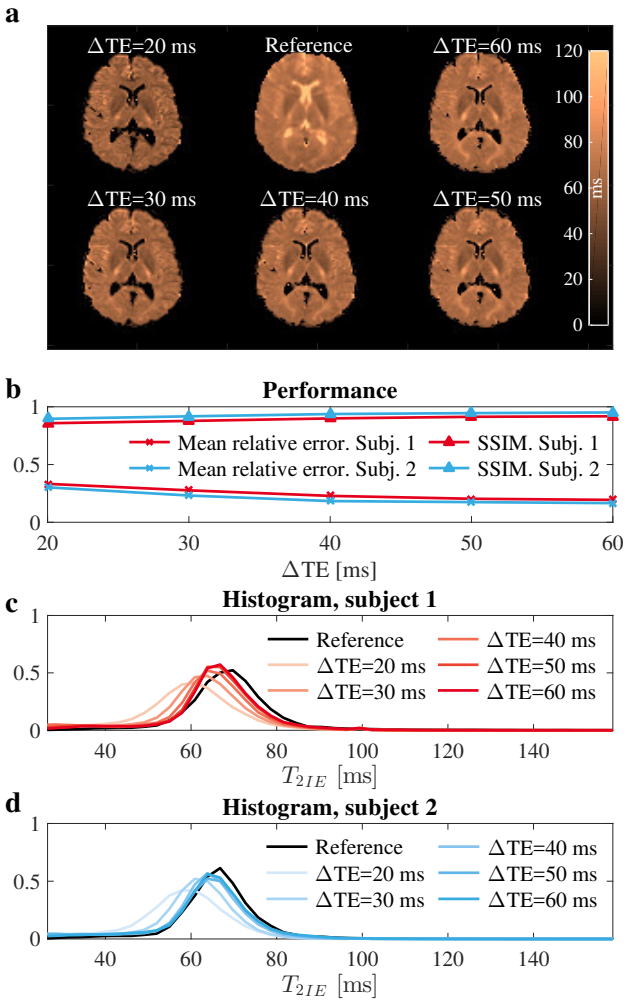

Figure 8: **Comparison of the BSS-estimated $T_{2_{IE}}$ values against a FLAIR reference.** A comparison of the reference (a, upper middle), for subject one with the BSS $T_{2_{IE}}$ estimate is shown for increasing values of ΔTE. The visual comparison was quantified by SSIM (50) and mean relative error (b). Histograms of the BSS-estimated $T_{2_{IE}}$ values are plotted against the reference (c) and (d). High T_2 values in the ventricles for the reference indicate that the suppression of the CSF signal in the FLAIR experiment was not perfect, although they appeared dark in the images (see supplementary Figure S20). This might have induced a positive bias for the reference. Finally, the BSS-estimated of $T_{2_{IE}}$ values for ΔTE above 50 ms showed good agreement with the reference.

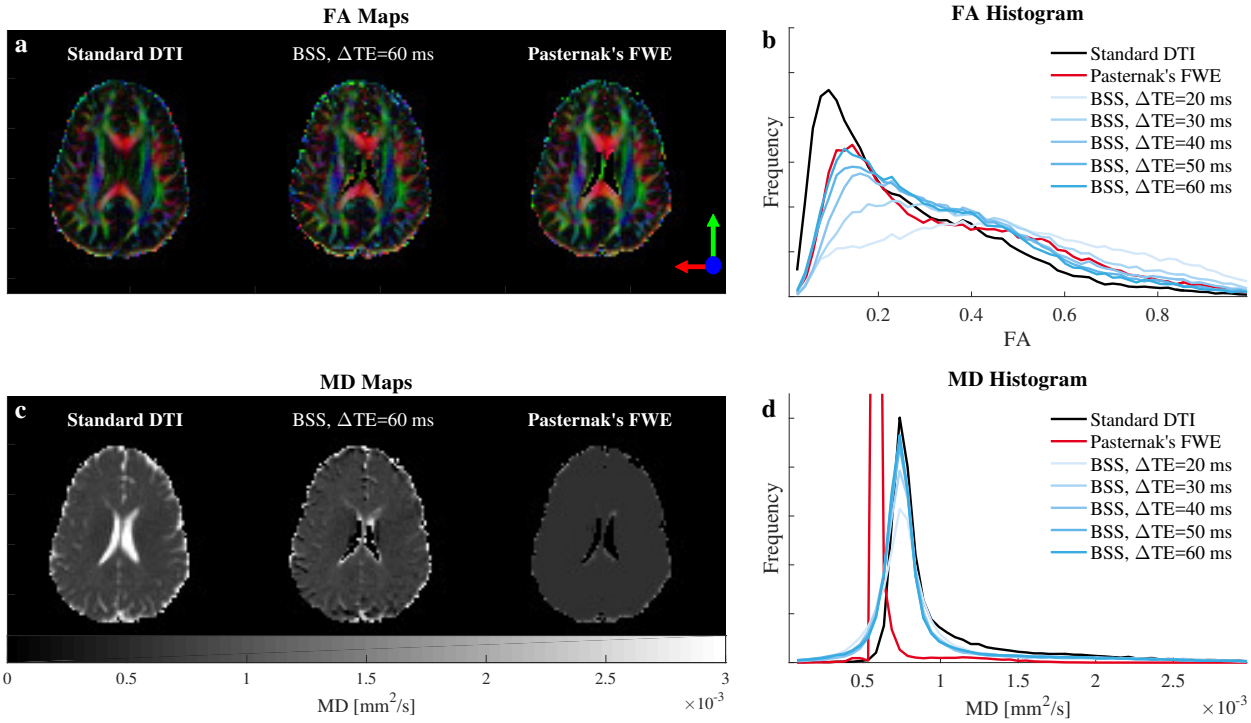

Figure 9: **FA and MD of the BSS-disentangled IE signal against the standard DTI and Pasternak's free-water elimination (FWE) for subject two.**

Comparisons of the FA (b) and MD (d) histograms calculated from the separated IE signals are plotted against the standard DTI fit and Pasternak's method for the short TE measured data. MD (c) and colored FA (a) maps are also included for comparison. We observed a CSF correction effect in the long ΔTE BSS for FA in agreement with Pasternak's FWE. However, both method disagree for MD, where Pasternak's introduces spatial over-regularization. See Figure S15 for the subject one.

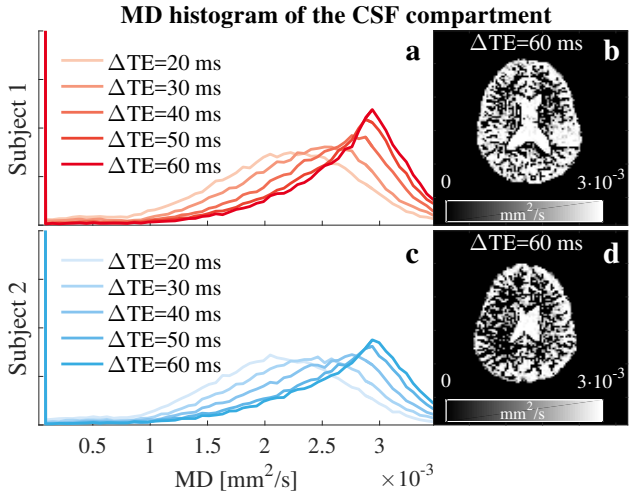

Figure 10: **Evolution of the MD histogram of the BSS-disentangled CSF component with ΔTE.**

The MD histograms, calculated from the the DTI fits for the signals disentangled for the CSF compartment, are plotted in (a) and (c). MD maps (b) and (d) are shown for anatomical inspection. The CSF MD histograms tends towards $3{\times}10^{-3}$ mm^2/s, in agreement with the literature.

Supporting Material

Phantom experiment

Methods

We built a phantom based on pure water and eleven different concentrations of agar and sucrose, producing eleven unique combinations of T_2 and diffusivity (Table S1) (62). We scanned the phantom (see below) and defined regions of interest (ROIs) in the tubes containing the eleven concentrations. Each ROI was independently processed with BSS to study the one compartment case. We also mixed the signals from two ROIs to generate a pair of two-compartment datasets and fed these to our BSS solver. Finally, for the three-compartment case we combined three ROIs and separated them with BSS. We were aiming to demonstrate that our framework was able to yield T_2 estimates for one compartment; and volume fraction, T_2 estimates and diffusion signal separation for two and three compartments.

For reference, we measured multi-echo SE acquisitions (Signa HDx 3T, GE Healthcare, Milwaukee, WI) for TE values from 10–640 ms in 10 ms increments. The following values were constant: TR = 3460 ms; NEX = 2; 128 × 128 matrix size; FOV = 240 mm; and 7 mm slice thickness. Eleven diffusion experiments were undertaken for TE values from 77.5–127.5 ms in 5 ms increments. the following parameters were constant: FOV = 240 mm; 7 mm slice thickness; 64 × 64 matrix size; TR = 4000 ms; ASSET = 2; A/P diffusion direction; and 41 equally spaced b-values from 0–2000 s/mm^2.

The multi-echo SE signals were averaged within each ROI. Each signal was fitted with NNLS (13) using a log-scaled grid with T_2 values at 500 points between 10–2000 ms. We used the maximum values of the NNLS T_2 spectra as ROI reference values (Figure S1) and fitted the signal from each ROI with EASI-SM (17) for reassurance.

One compartment

For one compartment ($M = 1$), we processed the diffusion data from ten pairs of TE measurements ($N = 2$) with BSS to include the relaxation effects in the dataset. For each pair, the short TE was fixed at 77.5 ms, while the long TE was increased from 82.5–127.5 ms along with the measured echo times. We constrained the solution space for the estimated $\hat{T}_2$ values to 10–2000 ms to account for all the ROIs. No other prior information was considered. We report the evolution of the T_2

values estimated using BSS for each ROI and the differences between the short and long TEs (ΔTE) compared with their reference values (Figure S1).

Two compartments

For two compartments ($M = N = 2$), we created two different datasets. First, we used the diffusion data measured at the shortest TE for ROI_6 and ROI_{11} as the sources, $\mathbf{S}$. These signals did not contain relaxation information (Figure S2a). Thus, to mix them together, we had to compute the mixing matrix ($\mathbf{A}$) as in in Eq. 2. We used their reference T_2 values, the experimental TEs, and a volume fraction of $f_{ROI_6} = 0.7$ (Figure S2c). We called this the *simulated* dataset, given that the signals were mixed under ideal conditions. Second, we normalized the measured data for each ROI and TE to its maximum value at the shortest TE to allow for later comparison of the volume fractions. In this case, the signals already contained the relaxation information (Figure S2b), so we did not need to compute $\mathbf{A}$. We scaled the normalized measured signals using the given volume fraction and added them together to create the mixed measurements, $\mathbf{X}$. We called this the *measured* dataset (Figure S2c). It accounts for system imperfections like signal drift, imperfect non-diffusion weighting, and eddy currents. To constrain the solution of the cALS algorithm we used $T_{2_{ROI_{11}}}$ and $S_{ROI_{11}}$ as the prior knowledge and searched for $\hat{T}_{2_{ROI_6}}$ between 0–200 ms.

Three compartments

We extended the two-compartments experiment to three ($M = N = 3$) by adding ROI_5. *Simulated* and *measured* datasets were created as for the two-compartments case (Figures S3a, S3b, S3c, S3d and S3e). This time, we used the volume fractions $f_{ROI_5} = 0.2$ and $f_{ROI_6} = 0.6$. To limit the solution space of the cALS algorithm, we assumed $T_{2_{ROI_{11}}}$ and $S_{ROI_{11}}$ to be prior the knowledge. We also constrained the $\hat{T}_{2_{ROI_5}}$ and $\hat{T}_{2_{ROI_6}}$ values to be between 0–50 ms, and 50–200 ms, respectively. For the two- and three-compartment experiments we report the stability of the framework, the relative error of the parameters and the disentangling capability of the method.

Results

One compartment

There was a correlation between the estimated T_2 values for one compartment obtained using multi-echo SE for 17 TEs and BSS for 2 TEs (Figures S1a, S1b, and Table S1). The T_2 estimates from

ROI_2 to ROI_{10} showed relative errors below 0.1 p.u. for a ΔTE of 50 ms (Figures S1a and S1b). The decreasing error trend is due to the relationship between the slope of a column of $\mathbf{A}$ and its T_2 value (Figure S1c). As ΔTE increased, the dynamic range of the slope of $\mathbf{A}$'s columns expanded, yielding better T_2 estimates. On the other hand, in Figures S1a and S1b, ROI_1 and ROI_{11} showed increasing errors as ΔTE increased. In the case of ROI_1, this was due to the low SNRs of the measurements at the experimental TEs. The noise floor caused changes in the signals for longer TEs that biased the T_2 estimates. The effect observed in ROI_{11} cannot be explained by SNR or T_2-slope dependence. We attribute this result to an underestimation of the reference T_2 value due to incomplete recovery of the longitudinal magnetization, which is caused by the short experimental TR (TR = 3460 ms) compared to the T_1 value of ROI_{11} ($T_{1_{11}}$ = 2200 ms). Finally, the error between the NNLS and BSS T_2 estimate for ROI_4, ROI_6, ROI_7, and ROI_8 is larger than for the others (Figure S1a) at ΔTE = 50 ms, except for ROI_1 and ROI_{11} already discussed. For these ROIs, NNLS converges to a bi-exponential decay (See Figure S19 and Table S1) increasing the value of the long T_2 coefficient compared to BSS and EASI-SM.

Two compartments

The disentangled signals for the *simulated* dataset replicated the profiles of the reference sources (Figure S2d). Moreover, the maximum relative errors for $\hat{f}_{S,ROI_6}$ and $\hat{T}_{2_{S,ROI_6}}$ were below 0.01 p.u. for all the possible ΔTE values. Interestingly, BSS was also able to separate the signal sources of the *measured* dataset (Figure S2d). This data accounted for non-ideal conditions due to system imperfections, such as signal drift, eddy currents, or imperfect non-diffusion weighting (Figure S2b, S2c, S2d, and S2f). In that case, the relative error in the $\hat{T}_{M_{S,ROI_6}}$ estimate remained under 0.1 p.u. for all ΔTEs above 10 ms. We believe that the 0.15 p.u. error in $\hat{f}_{M,ROI_6}$ is due to the differences between the *simulated* and *measured* signals at b = 0 s/mm^2, their influence on Eq. 4, and propagation of the error in the $\hat{T}_2$ estimate. Finally, we also observed a small stabilization effect in the volume fraction estimates as ΔTE increased (Figure S2f). This behavior is due to reductions in $\mathbf{A}$'s condition number improving the cALS algorithm's numerical stability (Figure S2e).

Three compartments

The condition number of $\mathbf{A}$ significantly increased compared with the two-compartment model (Figures S2e and S3g). Results for the *simulated* data (Figures S3a, S3e and S3f) showed that the signals for compartments ROI_6 and ROI_{11} had been separated, in agreement with their references.

Likewise, the relative errors in the $\hat{T}_{2_{S,ROI_6}}$ and $\hat{f}_{S,ROI_6}$ estimates were below 0.01 p.u., confirming the good separation. It is worth noting that the signal for the fast-decaying compartment (ROI_5) was detected, despite being heavily contaminated by the ROI_6. We believe that this result is due to the comparably large experimental TE, reducing its contribution to the observed signal. Equivalently, we found a 0.15 p.u. error in the $\hat{f}_{S,ROI_5}$ estimate and 0.45 p.u. in the $\hat{T}_{2_{S,ROI_5}}$ estimate.

Results for the *measured* data when **A**'s condition number was lowest showed that the signals from ROI_6 and ROI_{11} had still been separated, in agreement with the references (Figure S3f). However, the signal from ROI_5 was lost due to acquisition imperfections, bad conditioning of **A**, and small contributions of this compartment at the measured TEs. On the other hand, the $\hat{T}_{2_{M,ROI_6}}$ estimate was stability with a relative error of 11%. In contrast, $\hat{f}_{M,ROI_6}$ was more unstable due to the bad conditioning of the system and propagation of the error in the $\hat{T}_{2_{M,ROI_6}}$ estimate.

Repeatability and reproducibility

Following the simulations, phantom experiment, and in vivo studies for incremental ΔTE, repeatability and reproducibility analyses were conducted to demonstrate the stability and reliability of our method. In this supporting section we described the experimental setup and results, while the discussion remained in the main body of the paper.

Methods

Repeatability

A healthy volunteer (male, 28 years old) was scanned six times in a 3.0T GE MR750w scanner (GE Healthcare, Milwaukee, WI). For each repetition we acquired two diffusion PGSE EPI volumes with TE values 75.3 and 135.3 ms (ΔTE = 60 ms); FOV = 225 mm; 4 mm slice thickness; 22 slices; TR = 8000 ms; 96 × 96 matrix size; ASSET = 2; 30 directions; and one non-diffusion-weighted volume. Besides, one non-diffusion-weighted volume was acquired with reversed polarity at each TE. Finally, a FLAIR multi-echo sequence was acquired with the same geometrical prescription for TE = 20 – 260 ms in 30 ms increments; ASSET = 0; and TR = 8000 ms. An extra volume was acquired with reverse polarity at TE = 20 ms.

Diffusion and FLAIR data were processed with FSL Topup (63, 64) and Eddy (65) to correct for distortions. The long TE diffusion volume was registered to the short TE one with FLIRT and processed with BSS for two compartments (IE and CSF). We used literature CSF values ($T_{2_{CSF}} = 2$

s and $D_{CSF} = 3 \times 10^{-3}$ mm^2/s) as the prior knowledge, and constrained $T_{2_{IE}}$ between 0 – 200 ms. Then, the resulting tissue volume was fitted to the DTI model using standard linear regression (FSL FDT). For comparison, the distortion free short TE diffusion volume was also fitted to the DTI model and free-water corrected with Pasternak's method. Finally, FLAIR data were matched to a dictionary of mono-exponential decays from 0 – 300 ms with 1 ms increments.

We reported the FA and MD histograms for the six repetitions of the standard DTI fit for the short TE, IE BSS, and Pasternak's method (Fig S16a and b). The free-water correction effects were quantified dividing the histograms in sectors, and computing relative change per sector in the number of voxels of BSS and Pasternak's method reference to the standard DTI fitting (Fig S16d and e). FA histograms were split in four quarters, while MD in two sectors with threshold in the IE literature value (MD = 0.7×10^{-3} mm^2/s) (28). Statistical t-test analyses were conducted to determine the differences between BSS and Pasternak's FWE. Histograms of BSS $T_{2_{IE}}$ and FLAIR T_2 (Fig S16c) were compared by their peak and full width half maximum (FWHM) values (Fig S16f).

Reproducibility

Twenty healthy volunteers (8 females, 26 years old in average) were scanned in a 3.0T GE MR750 scanner (GE Healthcare, Milwaukee, WI) at the Max Planck Institute of Psychiatry in Munich, Germany. Two diffusion PGSE EPI volumes with TE values 60.1 and 120.1 ms (ΔTE = 60 ms) with TR = 5000 ms were acquired. All the other acquisition parameters and data processing steps were as described for the repeatability experiment. Due to scanner availability FLAIR data was only acquired for half of the subjects. Histograms of FA, MD, and T_2, along with their statistical analyses were reported in Figure S17.

Results

Repeatability

The histograms of FA, MD and T_2 (Figure S16a, b, and c) showed highly overlapping curves for each repetition and method, denoting good repeatability for all of them. After splitting the FA histogram in four sectors and computing the relative change in the area per sector for BSS and Pasternak's method (Figure S16d), we found that the lowest ratio between the mean and the standard deviation for BSS was 5.3 (sector IV) and 11.4 for Pasternak's (sector II). The fact that the mean is 5.3 larger

than the standard deviation suggested that BSS produces highly stable free-water correction. This result held also for MD, where we found ratios of 9.9 and 65.4 for BSS and Pasternak's method in sector II; and T_2, with mean to standard deviation ratios of 62.3 and 10.4 in the peak and FWHM values for BSS.

Interestingly, we found that BSS and Pasternak's free-water correction yield statistically different results for FA > 0.25 (sectors II, III, and IV, Figure S16d and e) and both MD sectors, with a significance level $\alpha = 0.01$. Finally, BSS $T_{2_{IE}}$ and FLAIR $T_{2_{IE}}$ histogram peaks were not statistically different, while the FWHM values were with a small effect. These findings indicate a good agreement of BSS with the FLAIR reference (Figure S16f).

Reproducibility

The FA, MD and T_2 histograms showed larger inter-subject variability (Figure S17a, b, and c) compared to the intra-subject one (Figure S16a, b, and c)) . The lowest ratios between the mean and the standard deviation of the free-water correction factor were 3.9 for BSS FA (sector IV) and 6.8 for Pasternak's FA (sector II); and 4.9 for BSS MD (sector II) and 20.5 for Pasternak's MD (sector II). Furthermore, mean to standard deviation ratios of BSS $T_{2_{IE}}$ were 47.2 and 8.9 for peak and FWHM values. These results suggested that BSS experiments are highly reproducible among subjects.

The statistical differences found in the repeatability study in FA sectors III and IV, and both MD sectors were still present in this analysis, indicating consistent differences between BSS and Pasternak's method (Figure S17d and e).

We found a statistically significant difference ($\alpha = 0.01$) between the means of the histogram peaks of the BSS and FLAIR $T_{2_{IE}}$ but with a small size effect (Figure S17f). Which indicates that BSS might yield a small bias in group comparisons compared to FLAIR multi-echo.

Supporting Figures (for publication)

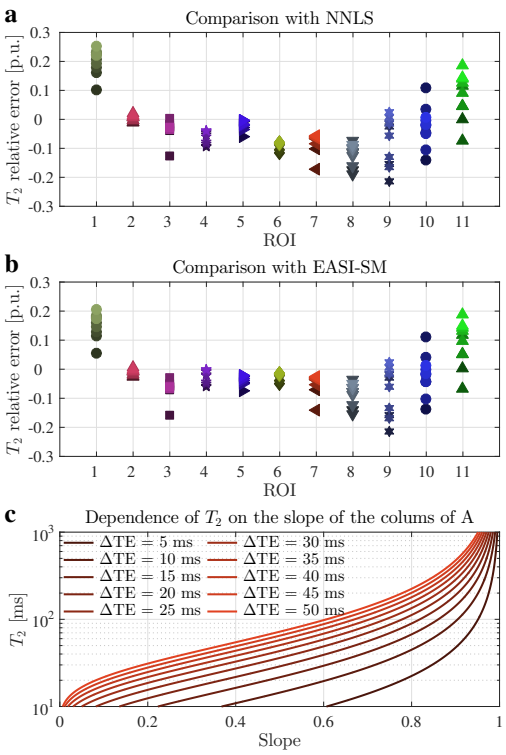

Figure S1: **Evolution of the relative error in the T_2 estimate with ΔTE for one compartment.**

The mean relative error of T_2 estimated using BSS is shown in (a) for NNLS and in (b) for EASI-SM references. ΔTE goes from 5 ms (darker colors) to 50 ms (lighter colors). The dependence of T_2 on the direction (slope) of the columns of $\mathbf{A}$ (Eq. 3) is shown in (c), where it can be seen how increasing ΔTE improves the dynamic range of the slope of $\mathbf{A}$, resulting in a better estimate for T_2. Except for ROI_1 and ROI_{11}, the remaining ones reduce the T_2 mean relative error as ΔTE increases (a and b, lighter colors are closer to zero), in agreement with plot c.

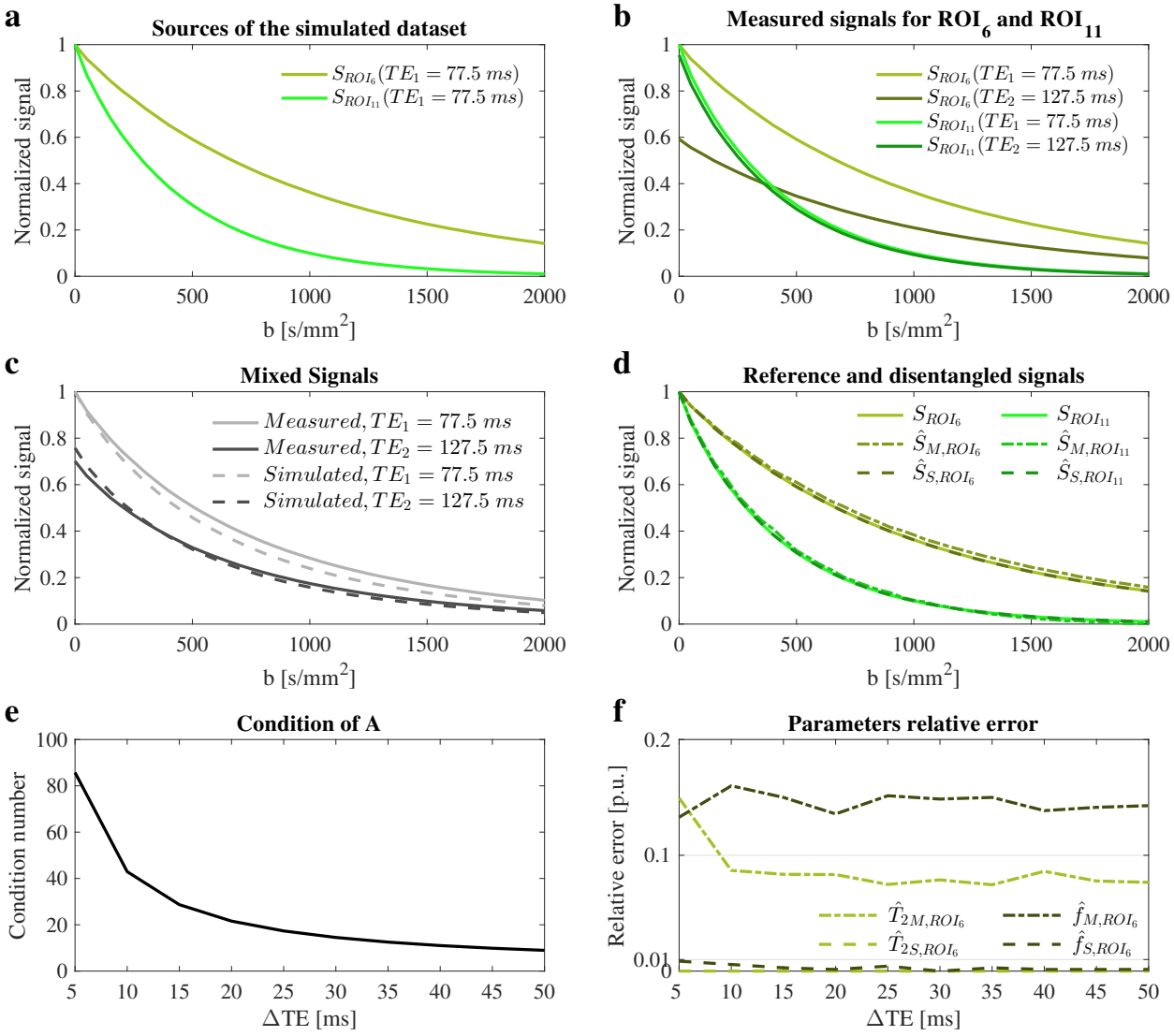

Figure S2: **Separation of two compartments and parameter estimation for the phantom data.**

The signal sources of the *simulated* dataset are plotted in (a), and the *measured* data generated from the sources in (b). The resulting mixtures for both datasets are shown in (c). We use the subscripts M and S to refer to estimates for the *measured* and *simulated* datasets, respectively. Measurement errors are highlighted by the differences between the *measured* and *simulated* signals, shown in (c). BSS disentangled the original sources for both datasets, as shown in (d). We chose a ΔTE of 50 ms to minimize the condition of $\mathbf{A}$ (shown in (e)) and increase the numerical stability of the framework. Finally, the relative errors in the estimated parameters, $\hat{T}_{2_{ROI_6}}$ and $\hat{f}_{ROI_6}$, are plotted in (f) for all possible values of ΔTE. We observed good agreement between the reference signals and those disentangled with BSS.

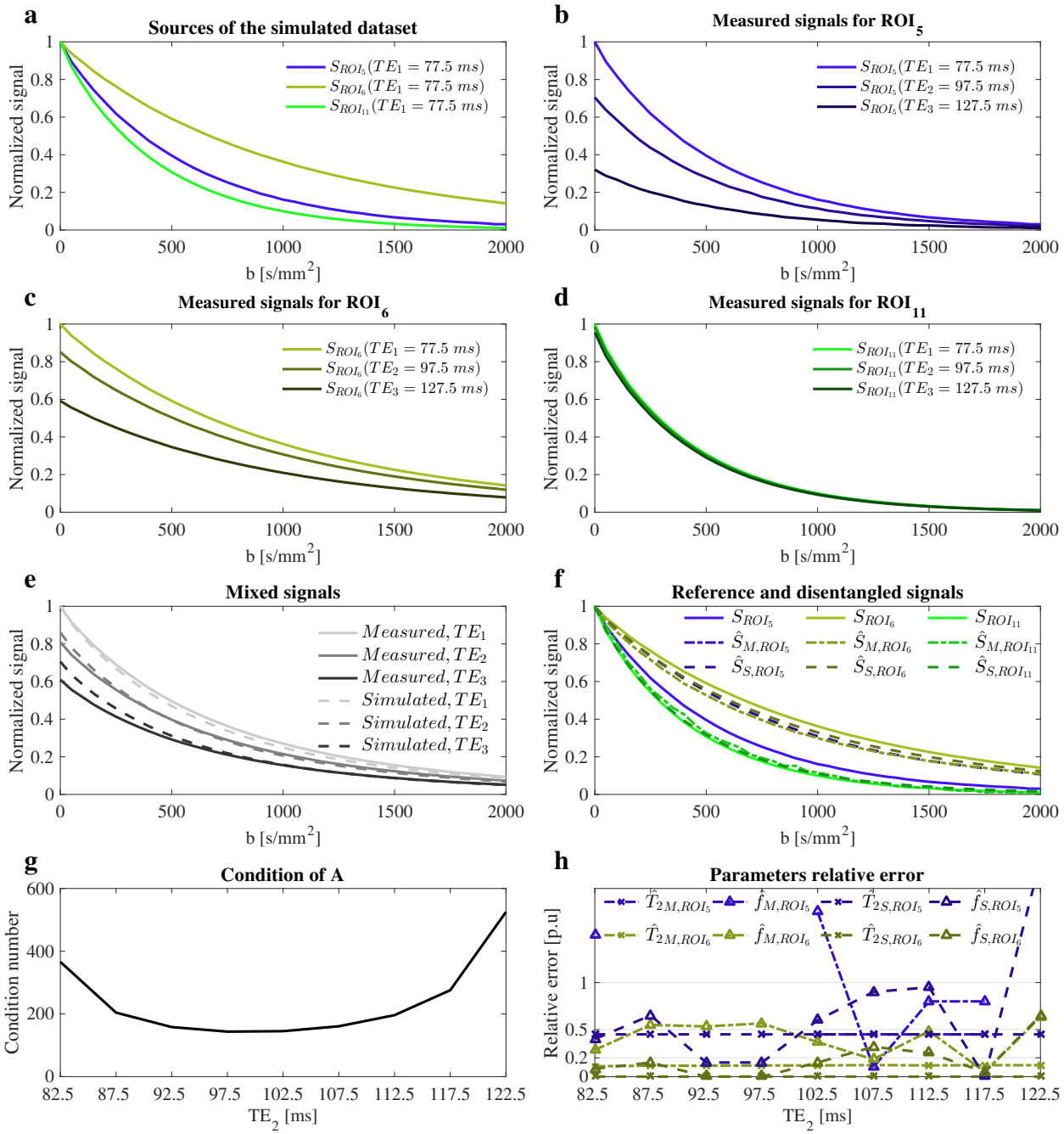

Figure S3: **Separation of three compartments and parameter estimation for the phantom data.**

The *simulated* dataset was generated from the signal sources in (a). The *measured* datasets were calculated from the measured signals for ROI_5 (b), ROI_6 (c), and ROI_{11} (d). The mixed signals for both datasets (shown in (e)) show a mismatch due to measurement errors. They were disentangled with BSS, as shown in (f). We fixed $TE_1 = 77.5$ ms and $TE_3 = 127.5$ ms, and varied TE_2 to minimize the condition number of $\mathbf{A}$ (shown in (g)). The relative errors of the estimated parameters are plotted for different values of the TE_2 in (h).

ROI	Agar [%]	Sucrose [%]	$T_{2_{EASI-SM}}[ms]$	$T_{2_{NNLS}}$ [ms]	$T_{2_{BSS}}$ [ms]	ϵ_{NNSL} [%]	$\epsilon_{EASI-SM}$ [%]
1	5	15	25.02	23.88 ± 1.92	29.9	25.37	19.61
2	5	5	31.59	31.13 ± 2.19	31.6	1.43	0.04
3	3	30	37.68	36.50 ± 3.04	35.4	2.95	5.99
4	3	15	106.23	110.07 ± 7.93	106.0	3.70	0.22
5	3	5	45.40	44.66 ± 2.85	44.5	0.40	2.02
6	1	30	95.46	102.19 ± 10.30	93.9	8.13	1.66
7	1	15	222.22	228.94 ± 12.15	216.3	5.53	2.67
8	1	5	225.19	233.85 ± 13.84	213.4	8.76	5.25
9	0	30	457.08	456.37 ± 26.50	467.6	2.47	2.31
10	0	15	395.95	397.56 ± 21.17	401.0	0.87	1.28
11	0	0.5	876.97	881.23 ± 64.07	1008.6	14.46	15.01

Table S1: **Phantom reference values and BSS estimates.**

The ROIs in the phantom experiment was built using the concentrations of agar and sucrose shown here. Signal decays along the diffusion dimension were compared to each other to ensure that they were all different, as required by BSS (see supplementary Figure S18). For reference, the T_2 values were characterized using an NNLS fit. Confidence intervals were taken at the half maxima of the NNLS spectral peaks. In addition, a second method, EASI-SM (17), was used to confirm the validity of the fits. Finally, the $T_{2_{BSS}}$ values were estimated for $\Delta\text{TE} = 50$ ms and compared with the NNLS and EASI-SM references (where ϵ refers to the relative error).

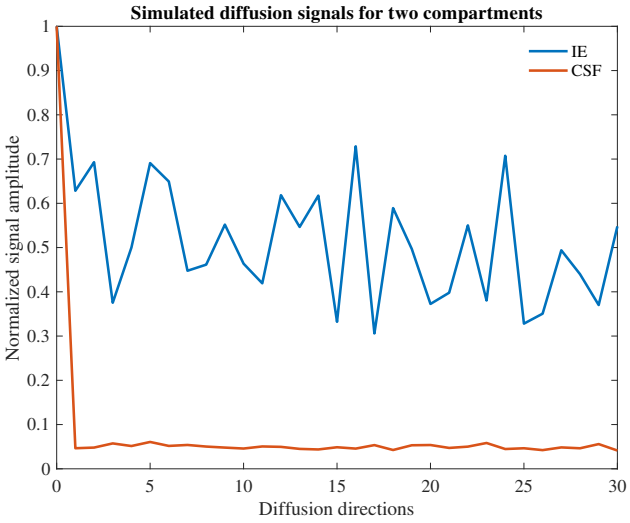

Figure S4: **Simulated diffusion signals for IE and CSF.**

Synthetically generated diffusion signals for 30 directions (b = 1000 s/mm^2) and one non-diffusion weighted measurement. We modeled diffusion as a Gaussian process with MD of IE and CSF equal to 0.7×10^{-3} and 3×10^{-3} mm^2/s respectively (28), and standard deviations of 0.3×10^{-3} and 0.1×10^{-3} mm^2/s respectively to distinguish between hindered anisotropic (IE) and free isotropic (CSF) diffusivity.

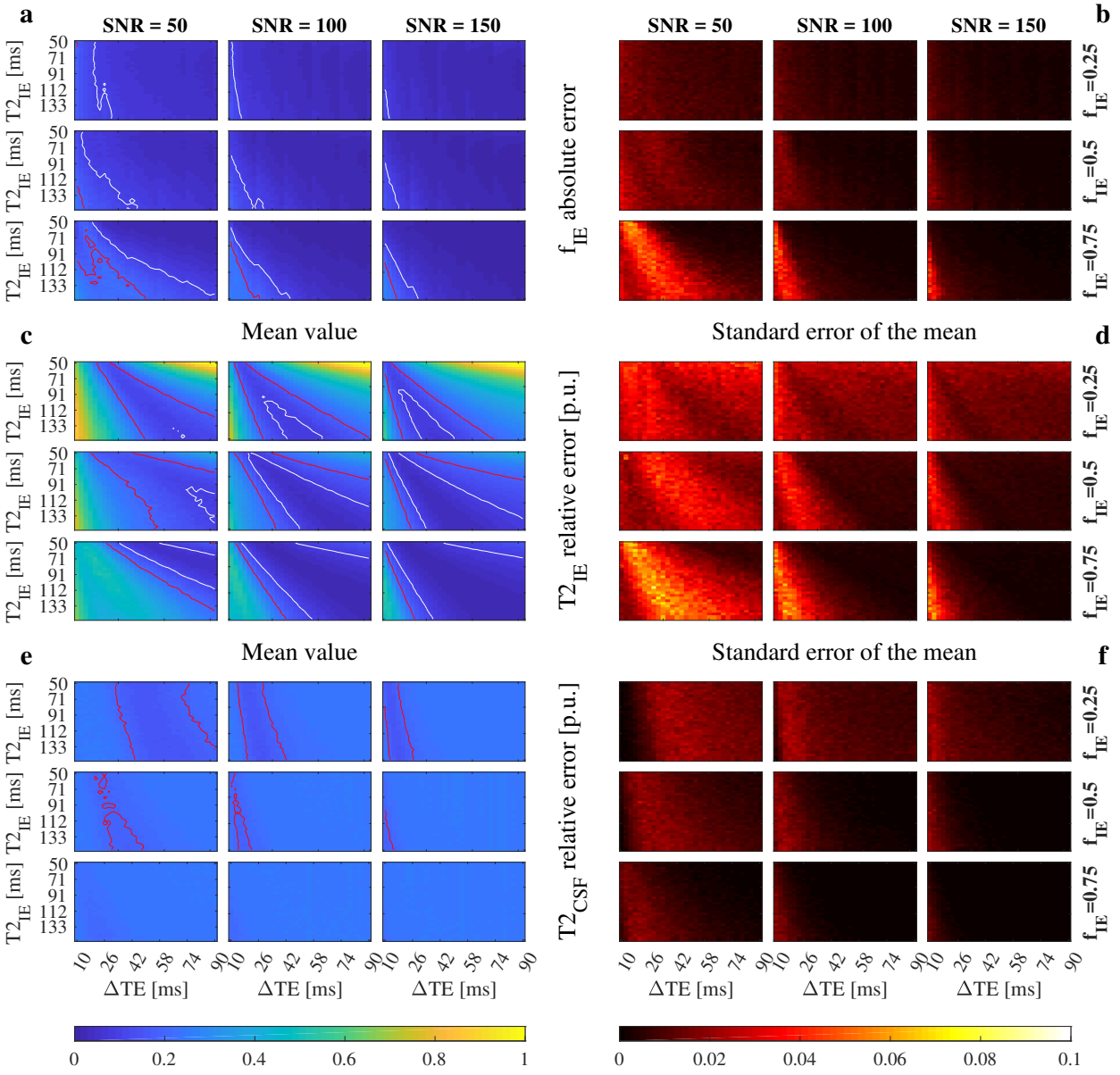

Figure S5: **Convergence for two compartments (IE and CSF) with overlapping T_2 constraints and no S_{CSF} prior.**

This figure extends the analysis of Figure 2 for SNR = 100 and 150. The stability for f_{IE} increases with SNR (a and b) and with f_{IE} for $T_{2_{IE}}$ (c and d).

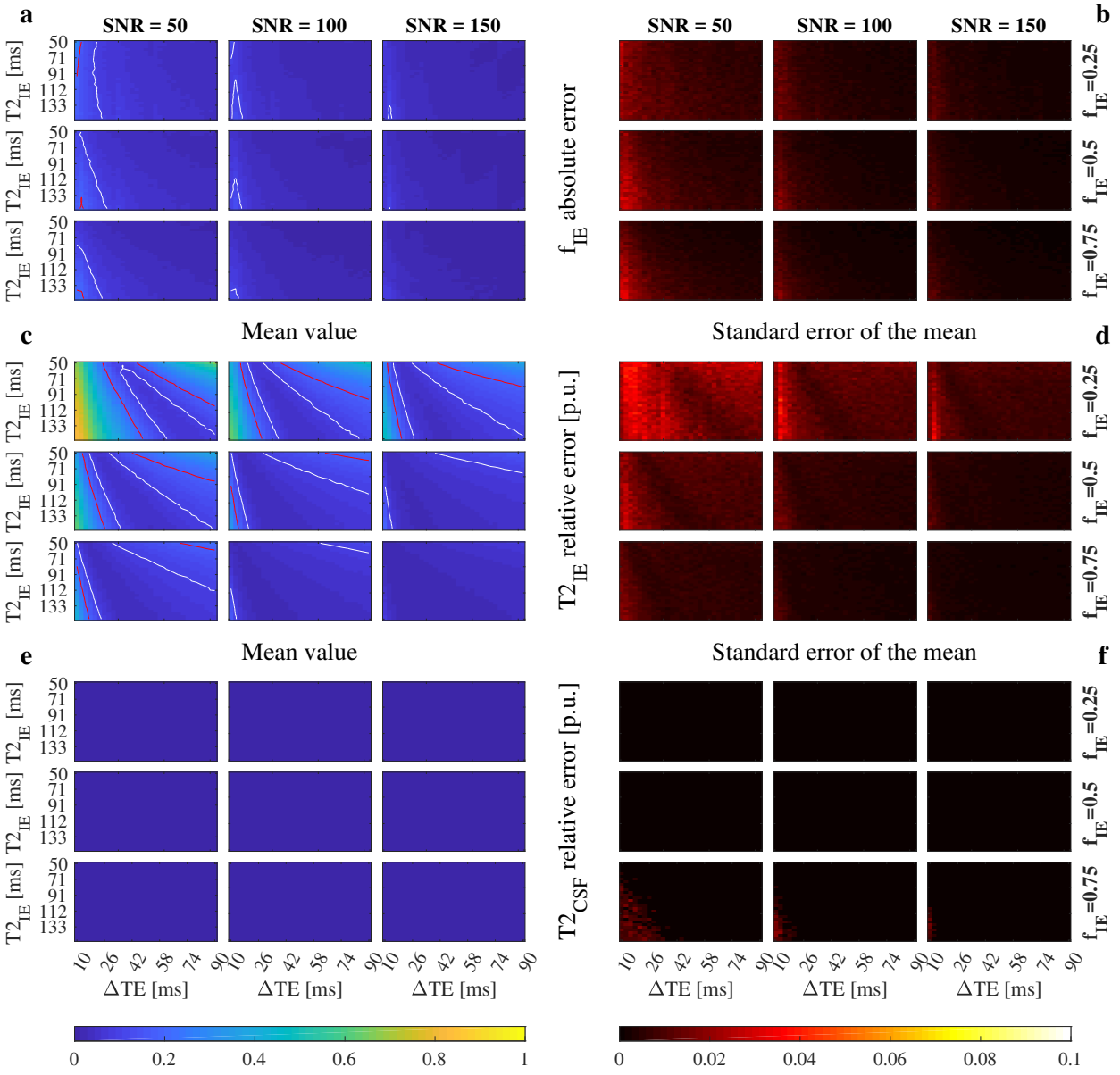

Figure S6: **Convergence for two compartments (IE and CSF) with non-overlapping T_2 constraints and S_{CSF} prior.**

This figure extends the analysis of Figure 3 for SNR = 100 and 150. The size and stability of the convergence area for f_{IE} and $T_{2_{IE}}$ increase with SNR.

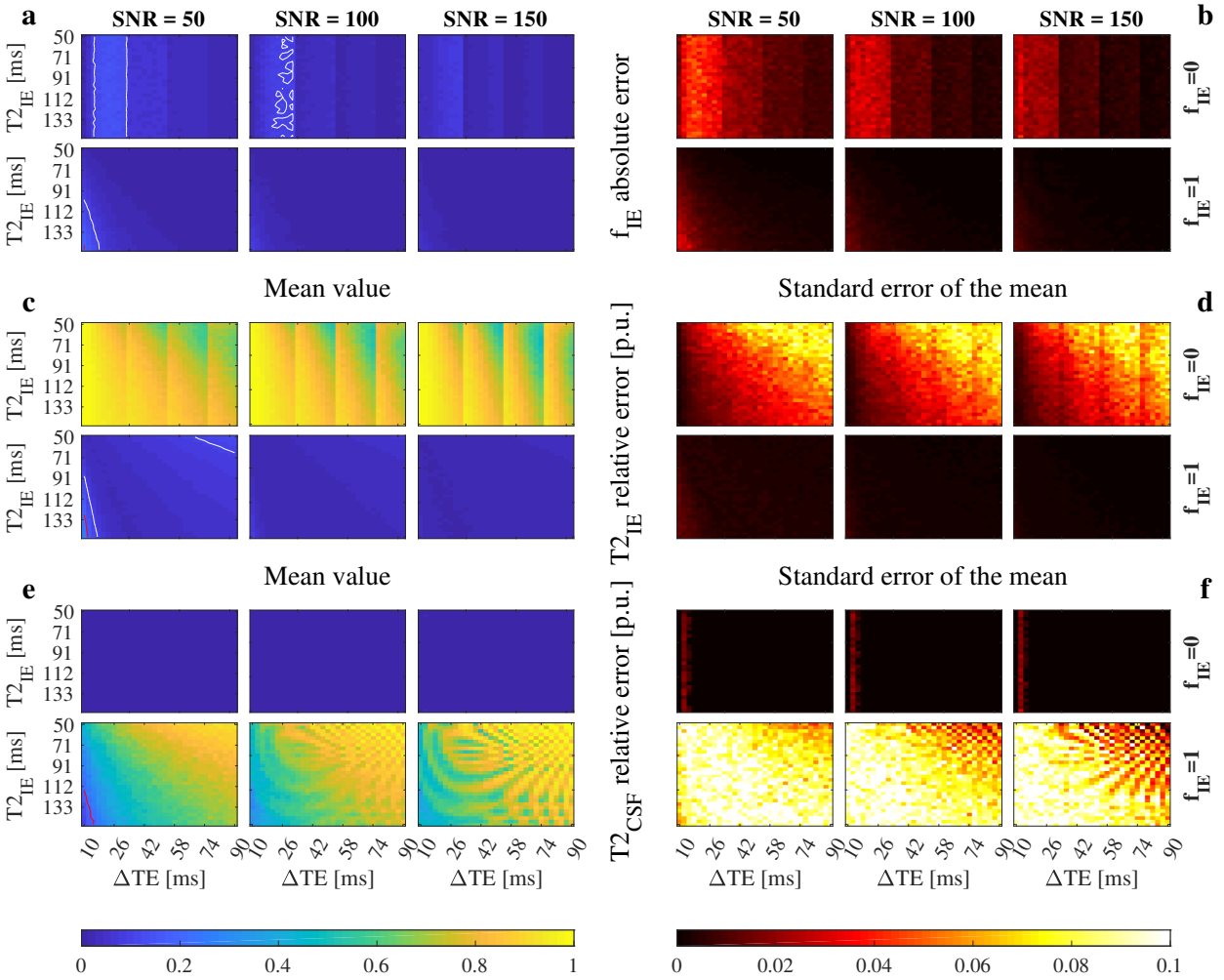

Figure S7: **Convergence for two compartments (IE and CSF) with non-overlapping T_2 constraints and S_{CSF} prior when only one is actually present in the tissue.**

This figure extends the analysis of Figure 4 for SNR = 100 and 150. The SNR does not play an important role in the definition of the convergence area.

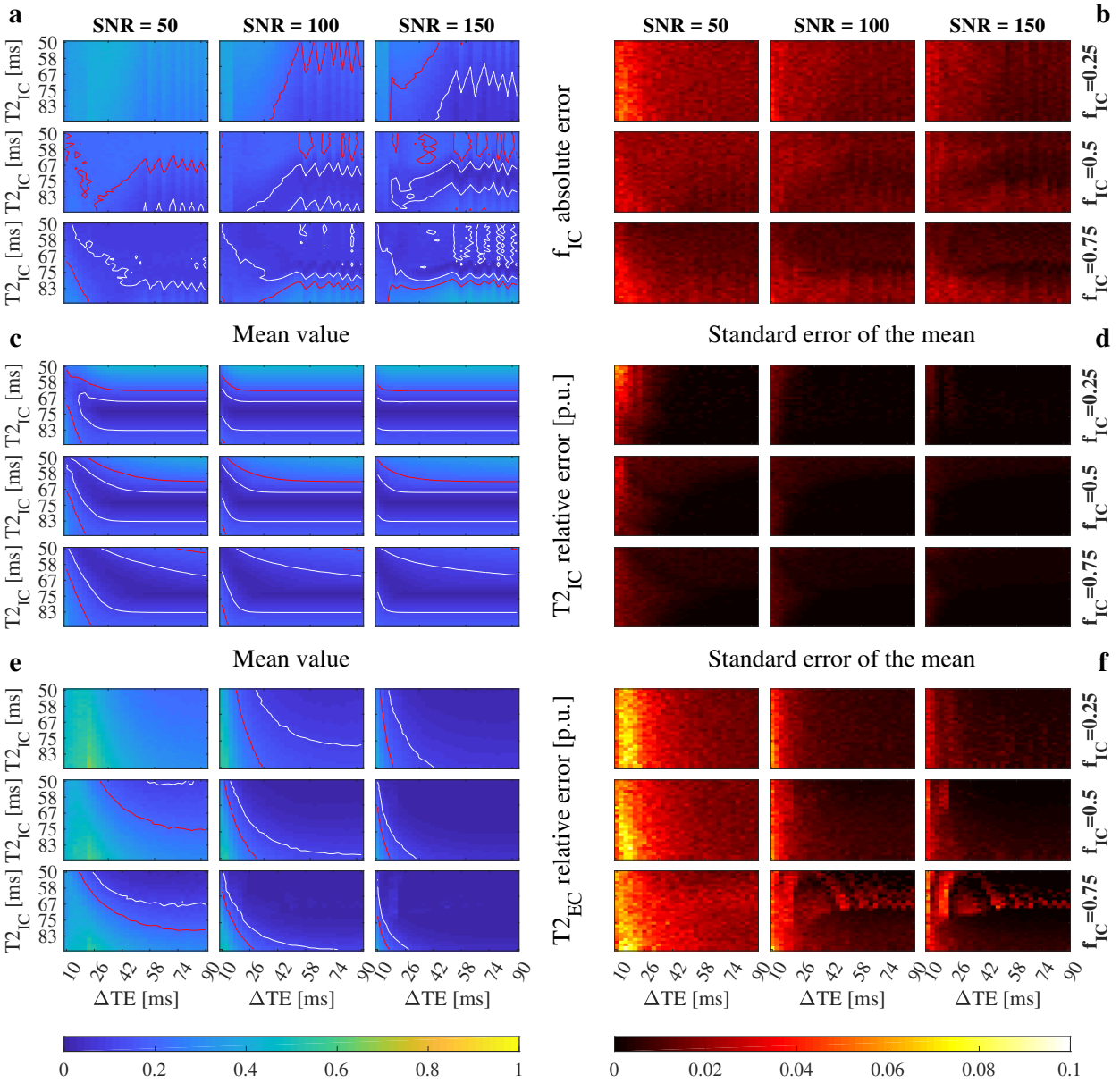

Figure S8: **Convergence for two compartments (IC and EC) with overlapping T_2 constraints and no other priors.**

This figure extends the analysis of Figure 5 for SNR = 100 and 150. The influence of SNR on f and $T_{2_{IC}}$ is small.

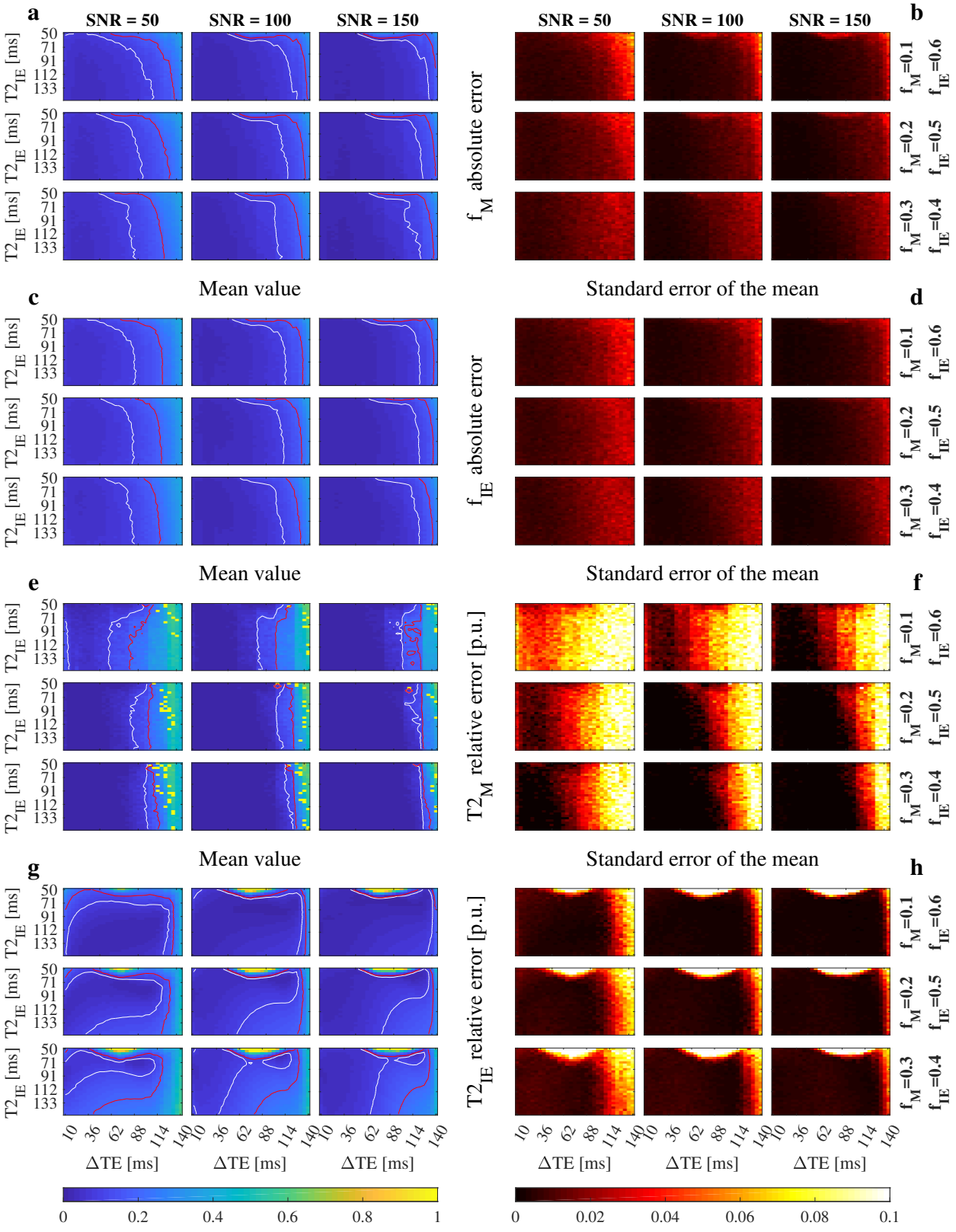

Figure S9: **Convergence for three compartments (myelin, IE, and CSF) with non-overlapping T_2 constraints and S_{CSF} prior.**

This Figure extends the analysis of Figure 6 for SNR = 100 and 150.

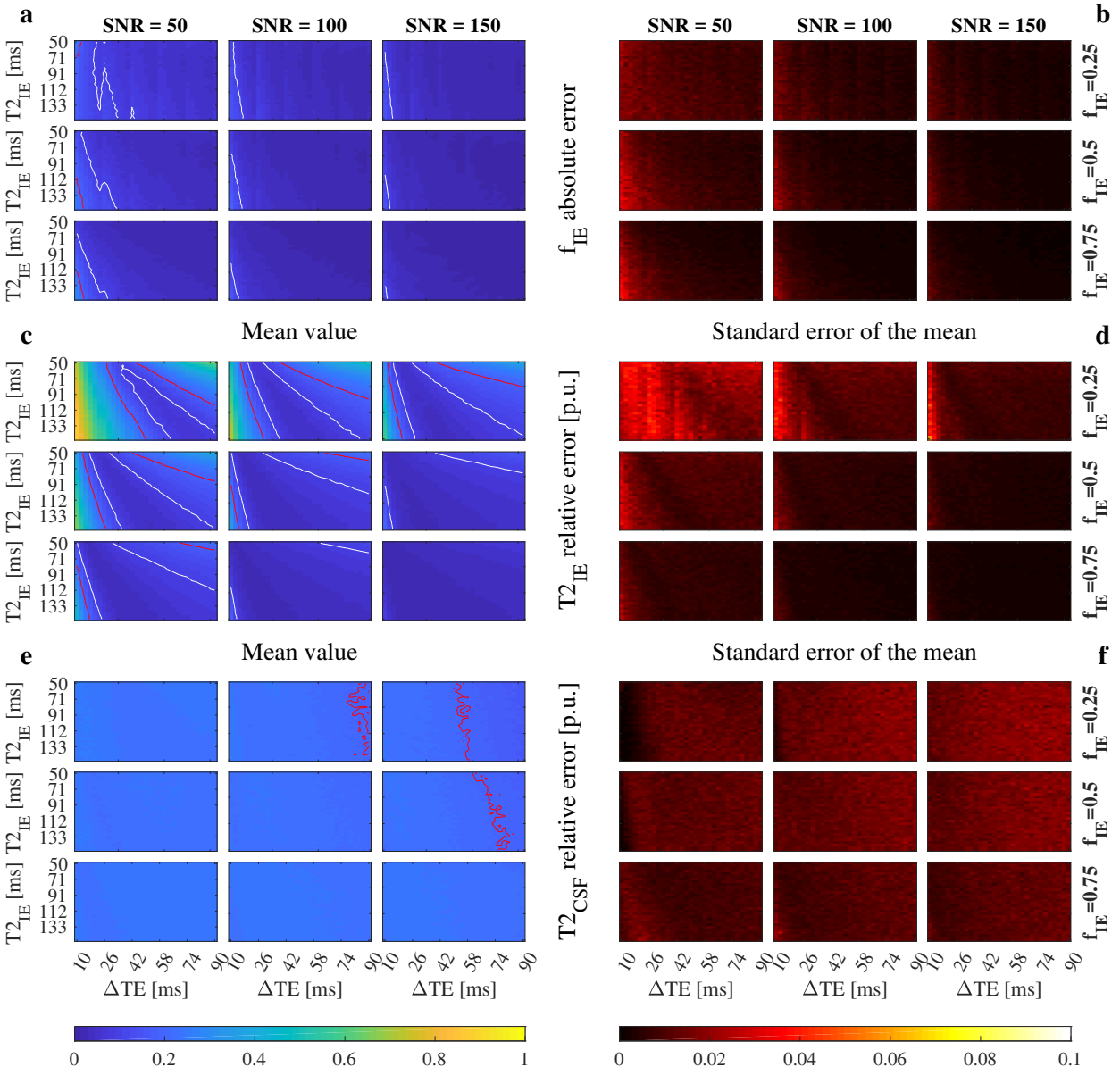

Figure S10: **Convergence for two compartments (IE and CSF) with overlapping T_2 constraints and S_{CSF} prior.**

The mean and the standard error of f_{IE} absolute error (a and b), and the mean and the standard error of $T_{2_{IE}}$ (c and d), and $T_{2_{CSF}}$ (e and f) relative error per unit (p.u.). Red and white lines mark the 0.2 and 0.1 contour respectively. One thousand simulations were run for each combination of SNR, f_{IE}, $T_{2_{IE}}$, and ΔTE. $T_{2_{IE}}$ and $T_{2_{CSF}}$ were bound between 0–1000 ms and 0–3000 ms respectively. S_{CSF} was set to have isotropic diffusivity with value 3×10^{-3} mm^2/s. We defined the convergence area as the one with error lower than 0.1 for f_{IE} and $T_{2_{IE}}$. Notice the growth of the converge area compared to the lack of priors (Figures 2 and S5).

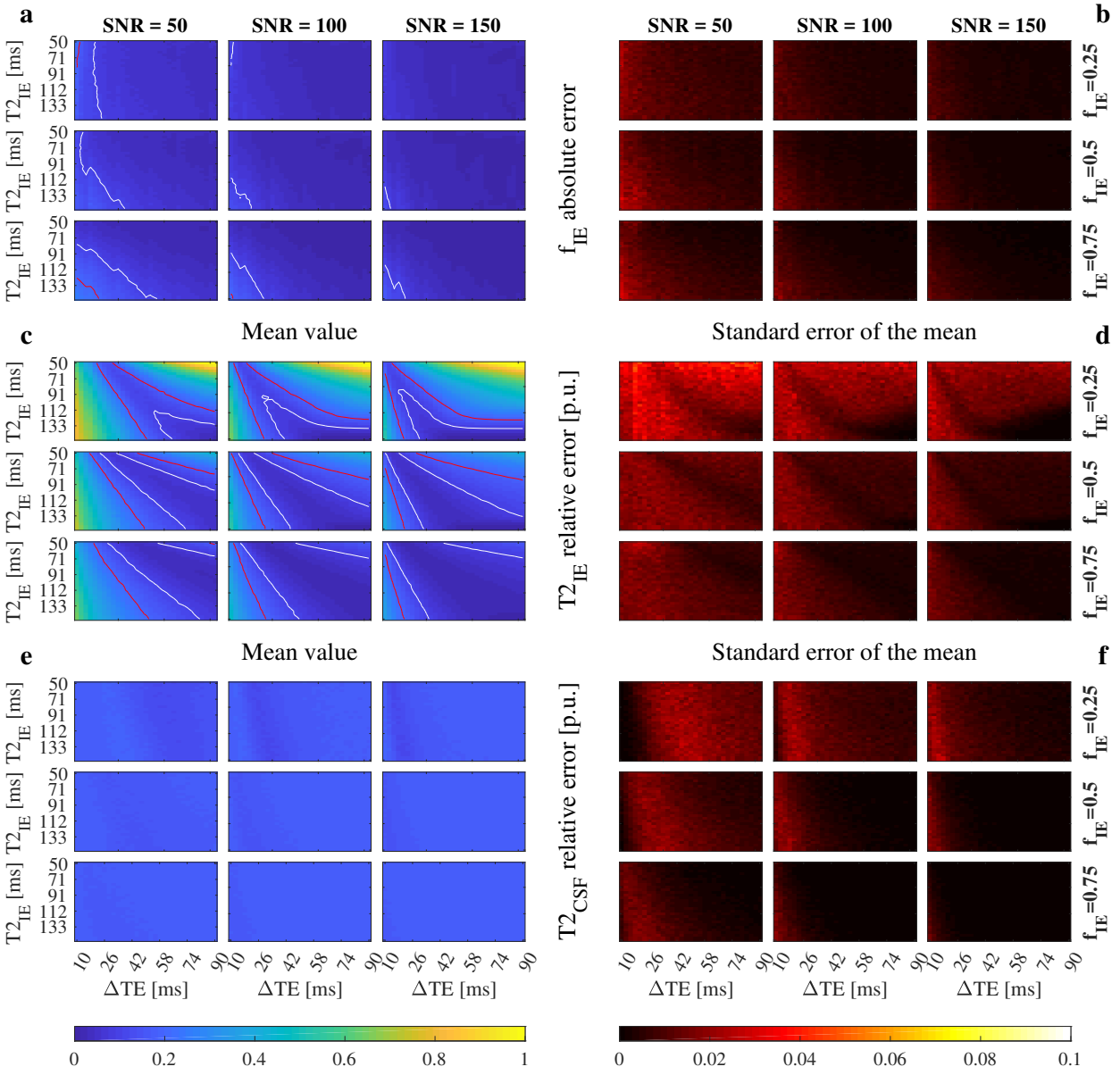

Figure S11: **Convergence for two compartments (IE and CSF) with non-overlapping T_2 constrained and no S_{CSF} prior.**

The mean and the standard error of f_{IE} absolute error (a and b), and the mean and the standard error of $T_{2_{IE}}$ (c and d), and $T_{2_{CSF}}$ (e and f) relative error per unit (p.u.). Red and white lines mark the 0.2 and 0.1 contour respectively. One thousand simulations were run for each combination of SNR, f_{IE}, $T_{2_{IE}}$, and ΔTE. $T_{2_{IE}}$ and $T_{2_{CSF}}$ were bound between 0–300 ms and 300–3000 ms respectively. No prior was imposed on S_{CSF}. We defined the convergence area as the one with error lower than 0.1 for f_{IE} and $T_{2_{IE}}$. Non-overlapping T_2 bounds stabilize the factorization, compared to Figures 2 and S5, although not as much as using priors on the signal sources (Figure S10).

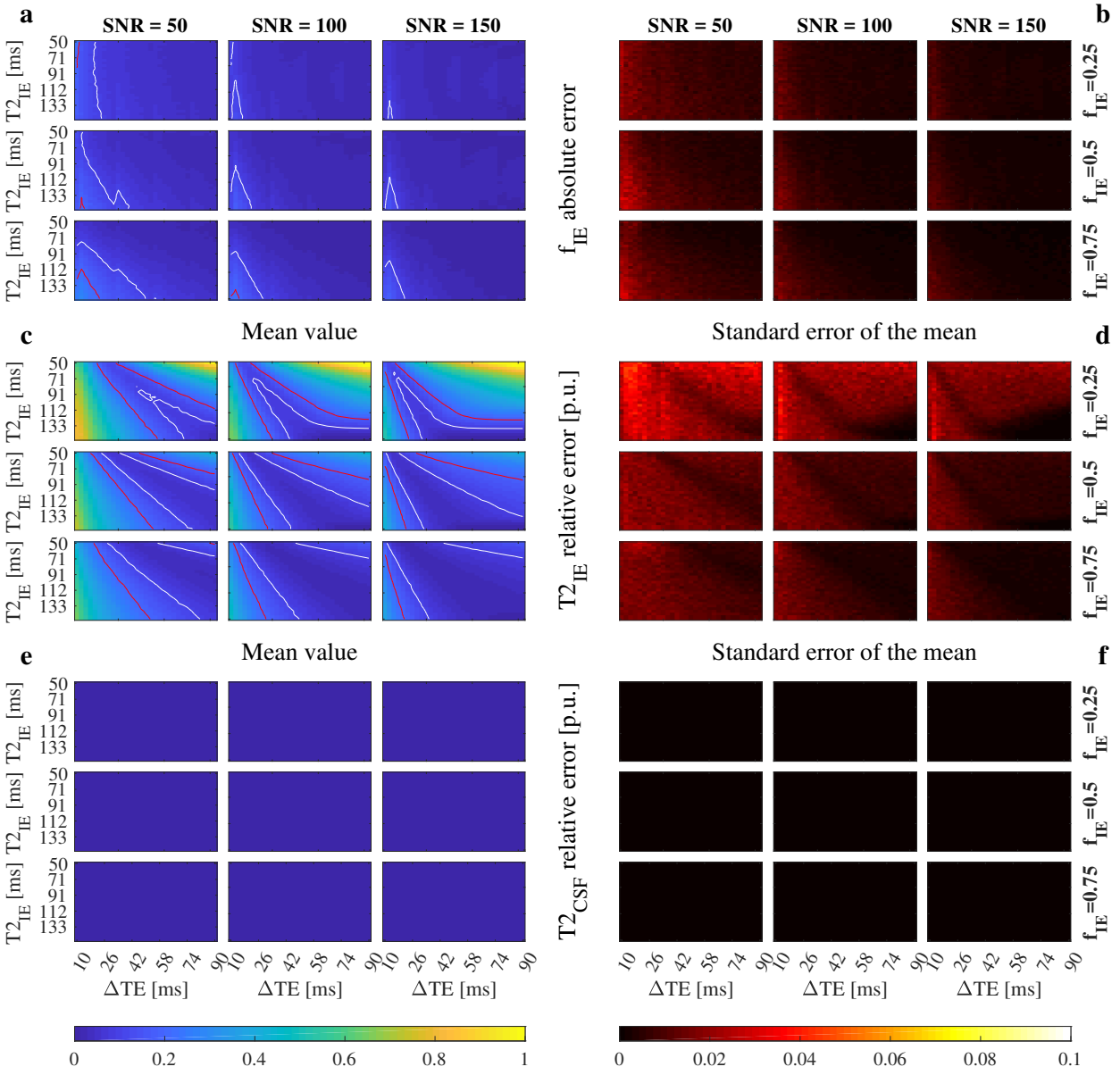

Figure S12: **Convergence for two compartments (IE and CSF) with fixed $T_{2_{CSF}}$ and no S_{CSF} prior.**

The mean and the standard error of f_{IE} absolute error (a and b), and the mean and the standard error of $T_{2_{IE}}$ (c and d), and $T_{2_{CSF}}$ (e and f) relative error per unit (p.u.). Red and white lines mark the 0.2 and 0.1 contour respectively. One thousand simulations were run for each combination of SNR, f_{IE}, $T_{2_{IE}}$, and ΔTE. $T_{2_{IE}}$ was bound between 0–300 and $T_{2_{CSF}}$ fixed to 2000 ms. No prior was imposed on S_{CSF}. We defined the convergence area as the one with error lower than 0.1 for f_{IE} and $T_{2_{IE}}$. Fixing the value of $T_{2_{CSF}}$ does not have any effect on the size of the convergence area, while bounding $T_{2_{IE}}$ does it (see Figure S11).

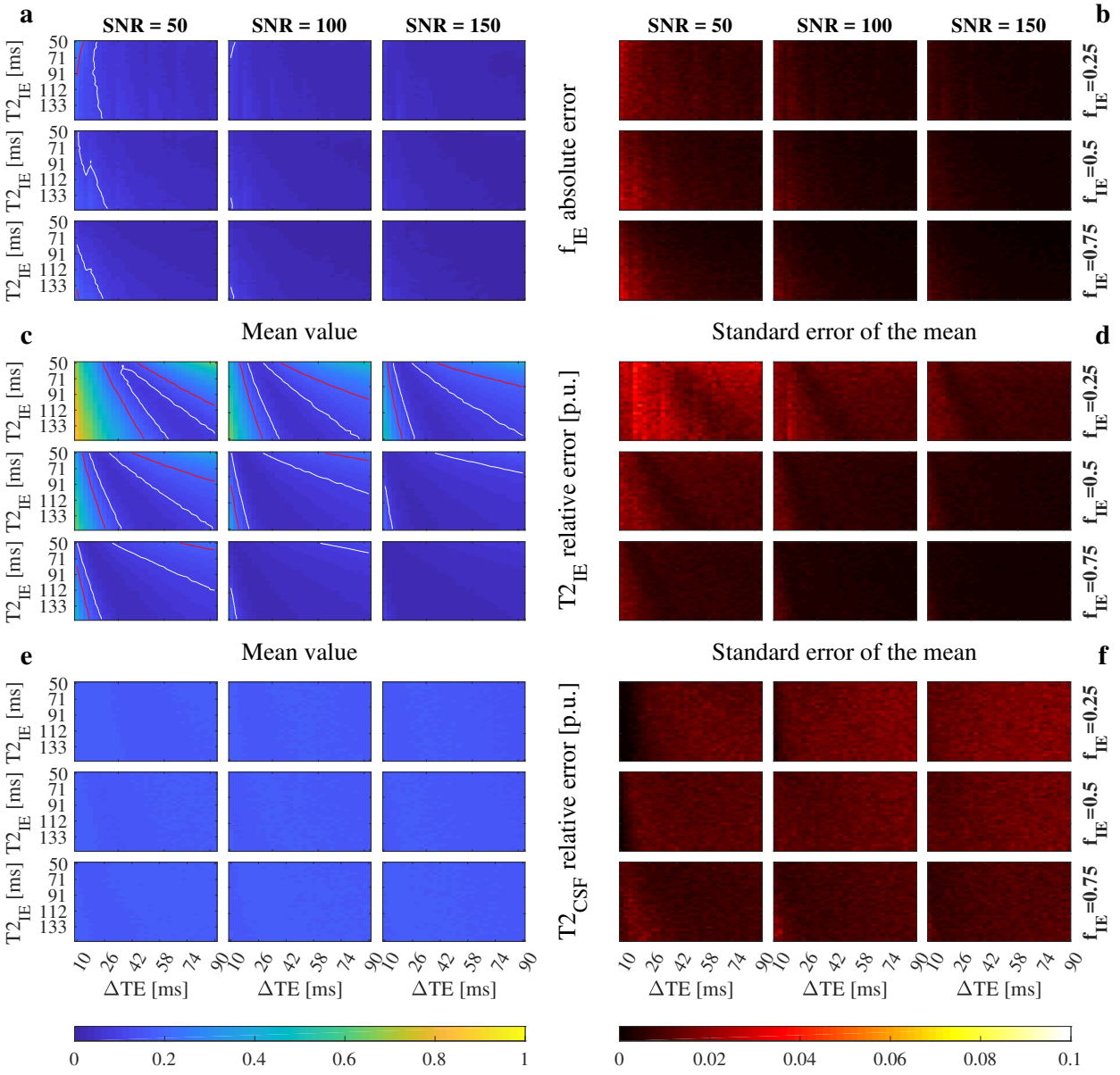

Figure S13: **Convergence for two compartments (IE and CSF) with non-overlapping T_2 constraints and S_{CSF} prior.**

The mean and standard error of f_{IE} absolute error (a and b), and mean and standard error of $T_{2_{IE}}$ (c and d), and $T_{2_{CSF}}$ (e and f) relative error per unit (p.u.). Red and white lines mark the 0.2 and 0.1 contour respectively. One thousand simulations were run for each combination of SNR, f_{IE}, $T_{2_{IE}}$, and ΔTE. $T_{2_{IE}}$ and $T_{2_{CSF}}$ were bound between 0–300 ms and 300–3000 ms respectively. S_{CSF} was set to have isotropic diffusivity with value 3×10^{-3} mm^2/s. We defined the convergence area as the one with error lower than 0.1 for f_{IE} and $T_{2_{IE}}$. Incorporating prior knowledge on the behavior of the signal sources (as CSF) improves convergence and stability more than bounding T_2 (Compare with Figures S10 and S11)

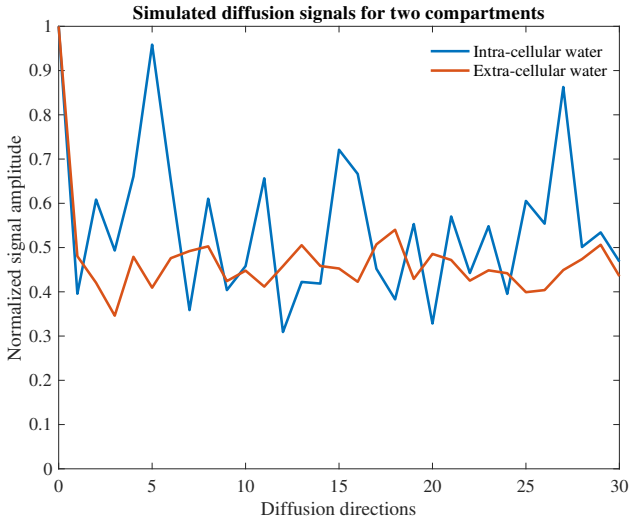

Figure S14: **Simulated diffusion signals for intra and extra-cellular water compartments.** Synthetically generated diffusion signals for 30 directions (b = 1000 s/mm^2) and one non-diffusion weighted measurement. We modeled diffusion as a Gaussian process with MD of intra-cellular (IC) and extra-cellular (EC) equal to 0.6×10^{-3} and 0.8×10^{-3} mm^2/s respectively (to keep the MD of parenchyma equals to 0.7×10^{-3} mm^2/s (28)) and standard deviations of 0.3×10^{-3} and 0.1×10^{-3} mm^2/s respectively to distinguish between a more (IC) and less (EC) hindered anisotropic diffusivity.

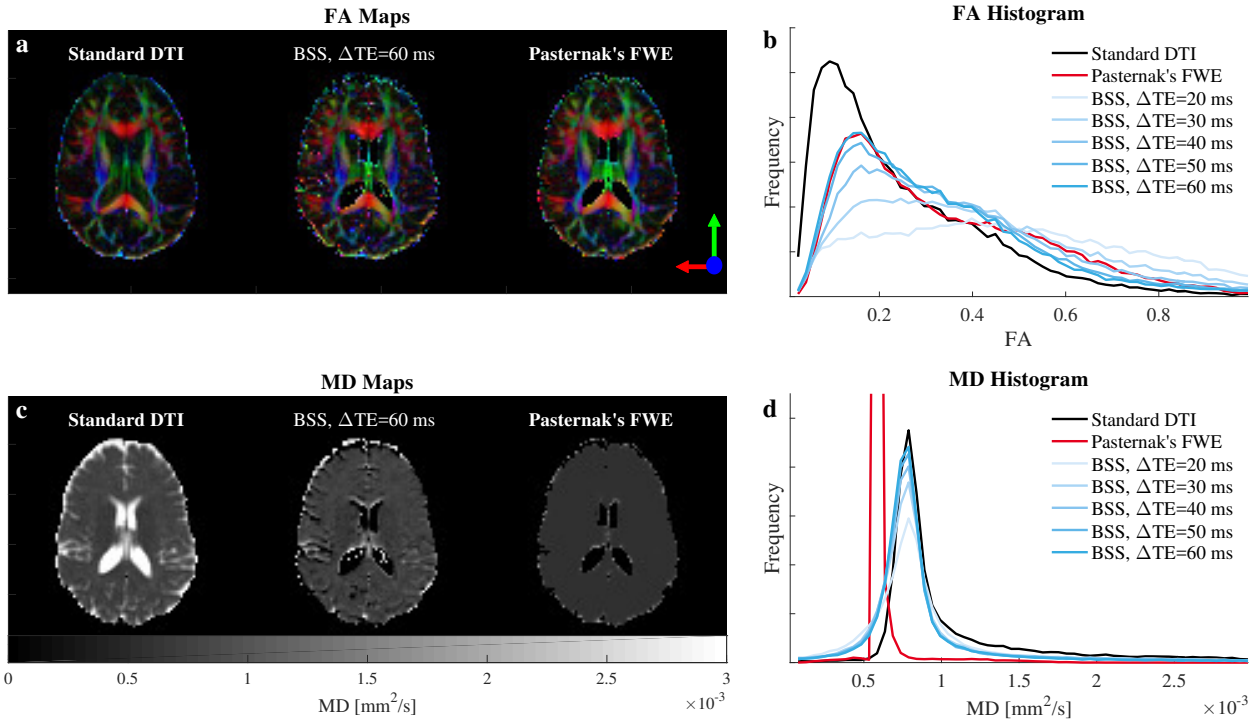

Figure S15: **FA and MD of the BSS-disentangled IE signal against the standard DTI and Pasternak's free-water elimination (FWE) for subject one.**

Comparisons of the FA (b) and MD (d) histograms calculated from the separated IE signals are plotted against the standard DTI fit and Pasternak's method for the short TE measured data. MD (c) and colored FA (a) maps are also included for comparison. We observed a CSF correction effect in the long ΔTE BSS for FA in agreement with Pasternak's FWE. However, both method disagree for MD, where Pasternak's introduces spatial over-regularization. See Figure 9 for subject two.

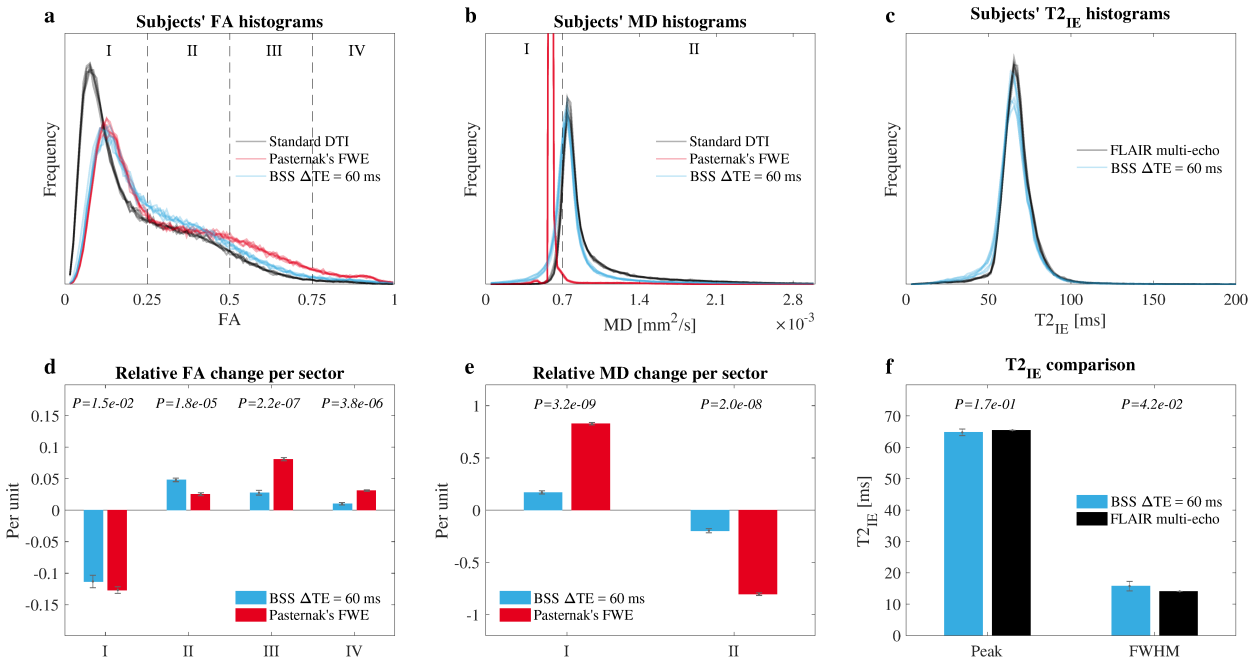

Figure S16: **Repeatability analysis showing intra-subject variability.**

A healthy volunteer was scanned six times. The FA (a) and MD (b) histograms for standard DTI, BSS and Pasternak's method are shown. These histograms were fragmented in sectors and the relative changes in number of voxels per sector and repetition for BSS and Pasternak's methods were computed. Statistical t-tests were run per sector to determine the level of significance of the differences between BSS and Pasternak's results (d and e). BSS and FLAIR $T_{2_{IE}}$ histograms (c) showed good agreement. Their peak and the full width half maximum (FWHM) were used for t-test comparison between BSS and FLAIR (f) highlighting the concordance.

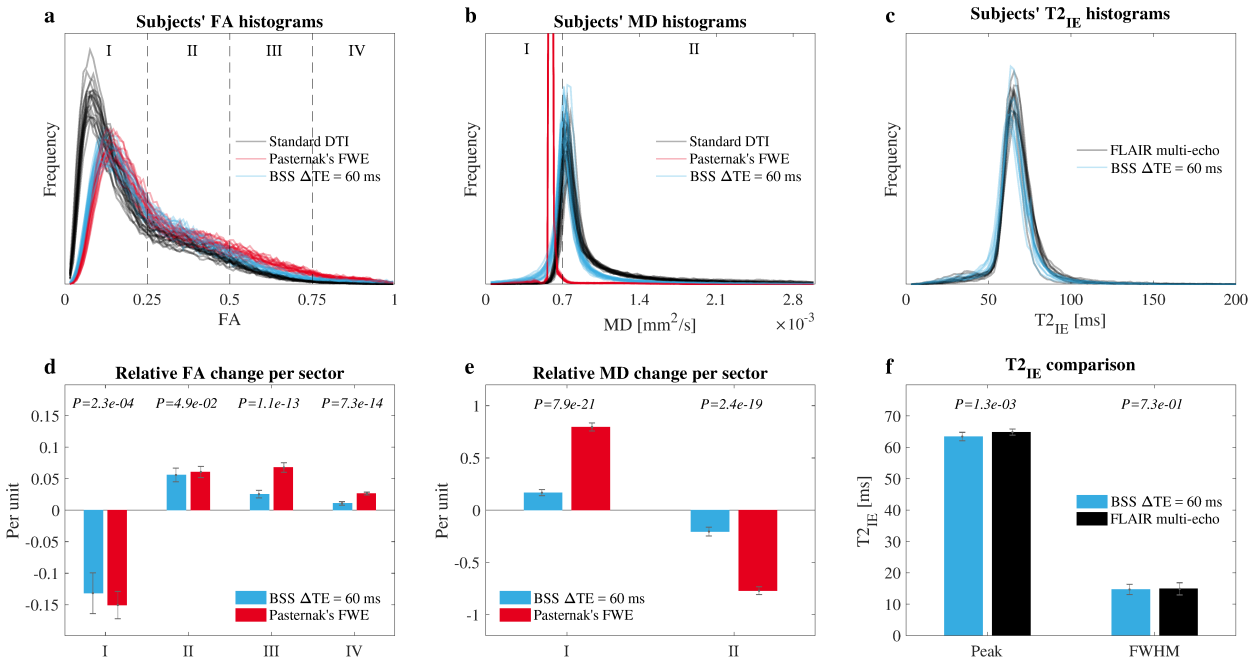

Figure S17: **Reproducibility analysis showing inter-subject variability.**

Twenty healthy volunteers were scanned. The FA (a) and MD (b) histograms for standard DTI, BSS and Pasternak's method are shown. These histograms were fragmented in sectors and the relative changes in number of voxels per sector and repetition for BSS and Pasternak's methods were computed. Statistical t-tests were run per sector to determine the level of significance of the differences between BSS and Pasternak's results (d and e). Notice that the inter-subject variability is larger than intra-subject (Figure S16). BSS and FLAIR $T_{2_{IE}}$ histograms (c) were depicted. Their peak and the full width half maximum (FWHM) were used for t-test comparison between BSS and FLAIR (f).

Supporting Figures only for reviewers

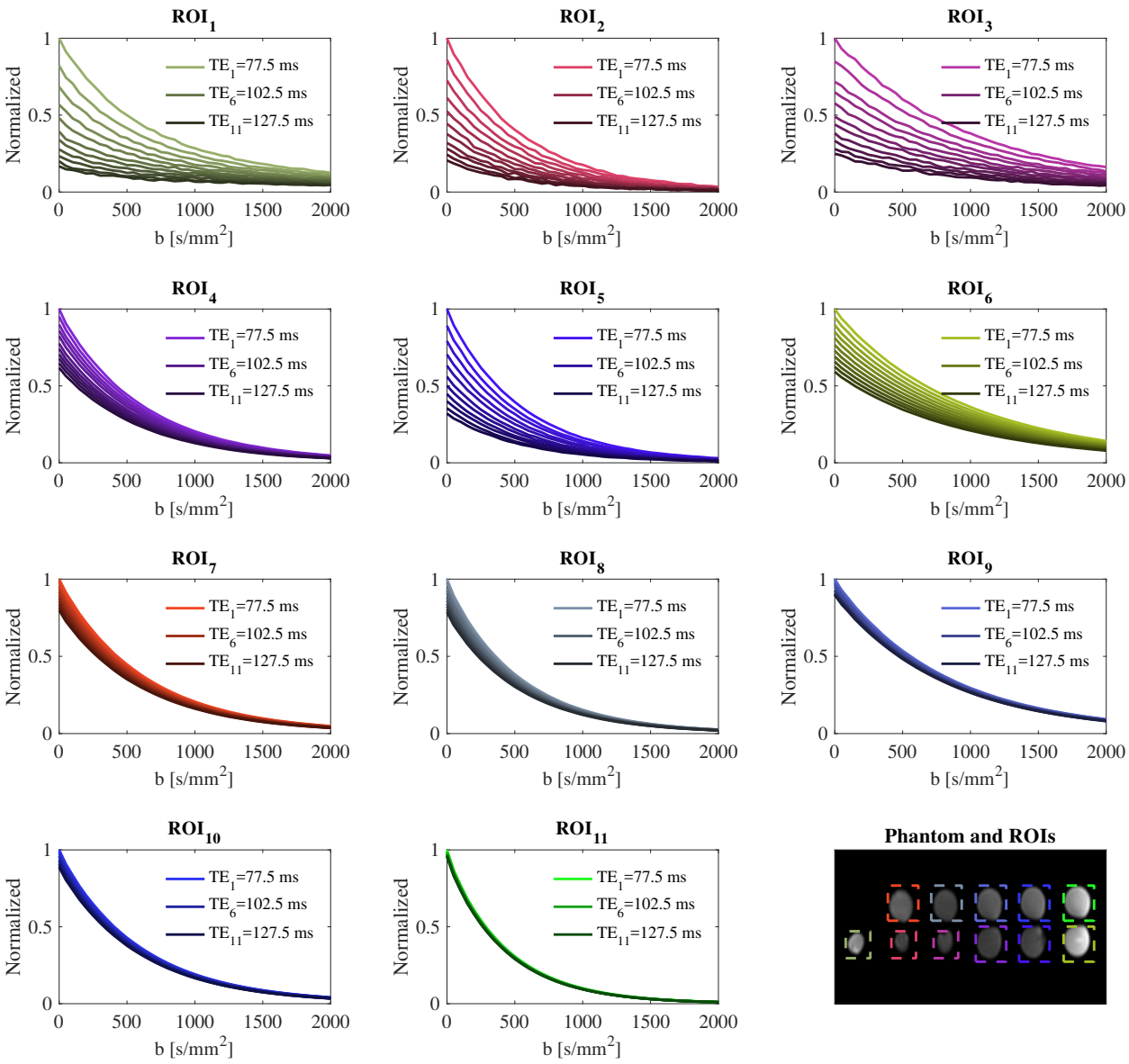

Figure S18: **Normalized diffusion signal decay profiles for all ROIs at each TE.** For reference, the measured signals for all ROIs at all TEs are shown here. The signals for shorter TEs are plotted in light colors, while longer TEs are represented by dark colors. Eleven TEs were measured from 77.5–127.5 ms in 5 ms increments. The phantom is shown alongside the ROIs in the lower right plot. Each ROI has a characteristic diffusion and relaxation signal decay profile.

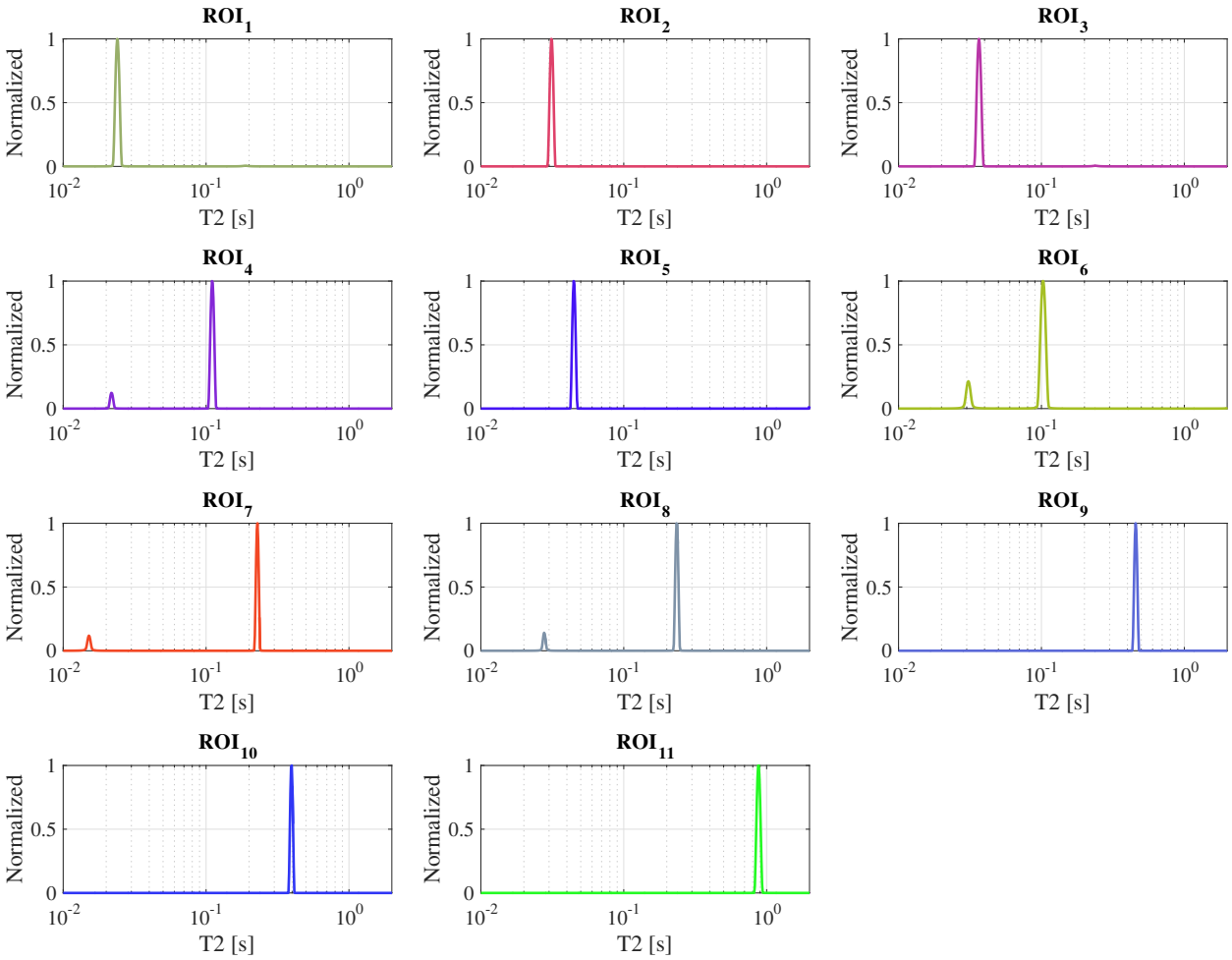

Figure S19: **Normalized NNLS spectrum for all ROIs.**

We The NNLS spectrum fitted for 500 T_2 points logarithmically spaced between 10 – 2000 ms. Notice the bi-exponential profile of ROI_4, ROI_6, ROI_7, and ROI_8.

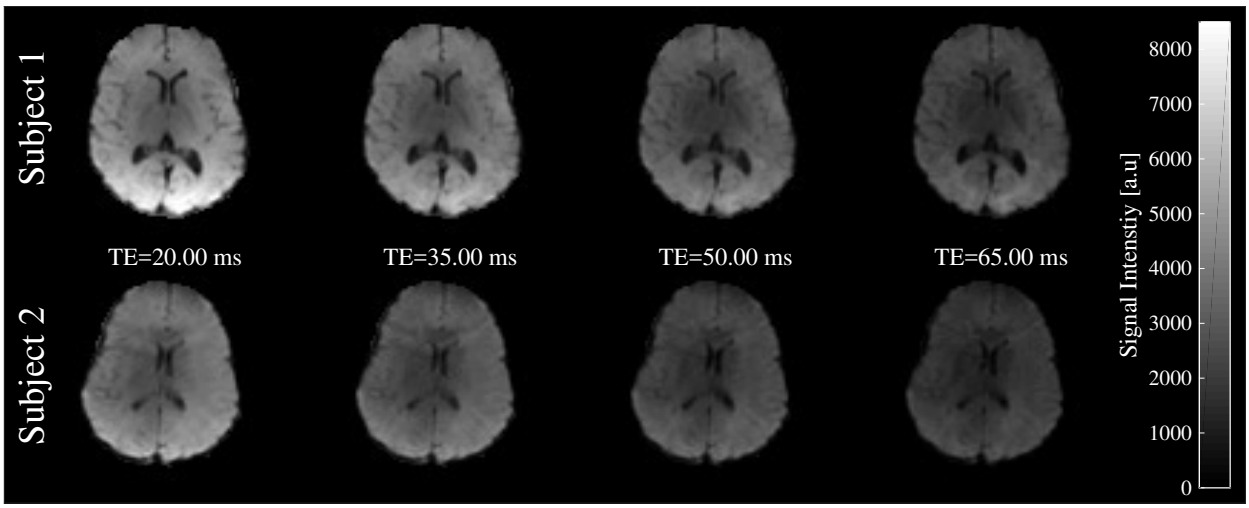

Figure S20: **FLAIR EPI images for both subjects at different echo times.**
We measured FLAIR EPI images for both subjects for TEs from 20–260ms in 15 ms increments. The shortest four TEs are shown for both subjects. The signal intensity in the ventricles is dark, indicating attenuation of the CSF component.

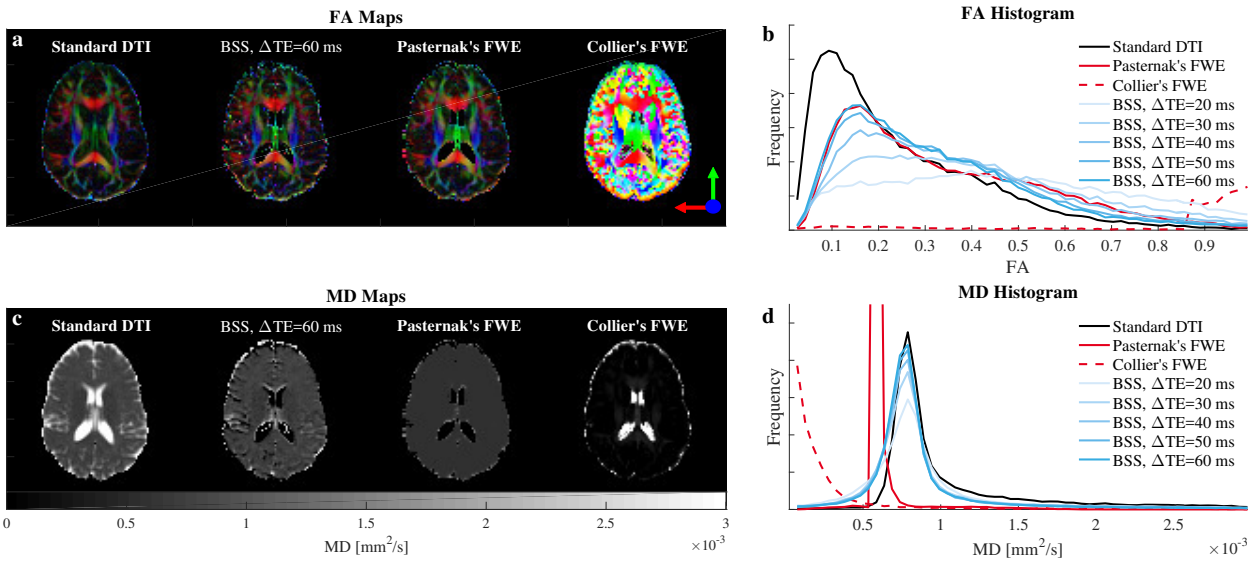

Figure S21: **FA and MD of the BSS-disentangled IE signal against the standard DTI fitting, Pasternak's, and Collier's free-water elimination (FWE) for subject one.** Comparisons of the FA (b) and MD (d) histograms calculated from the separated IE signals are plotted against the standard DTI, Pasternak's, and Collier's method fit for the short TE measured data. MD (c) and colored FA (a) maps are also included for comparison. We observed a CSF correction effect in the long ΔTE BSS for FA in agreement with Pasternak's FWE. However, both method disagree for MD, where Pasternak's introduces spatial over-regularization. Collier's method did not converge for our single-shell acquisition.

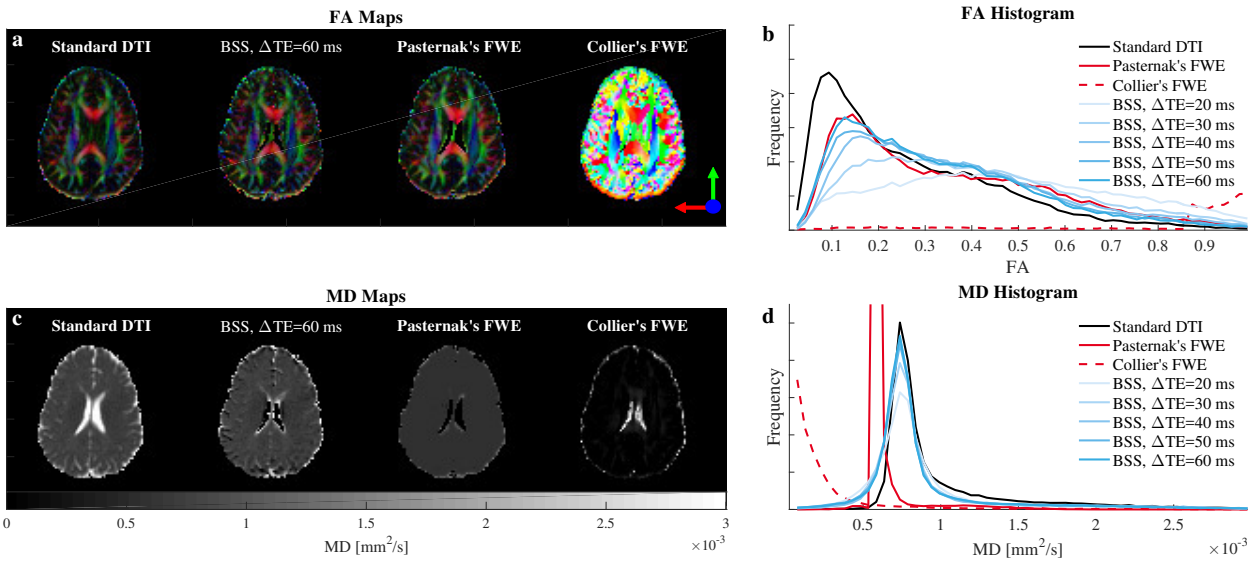

Figure S22: **FA and MD of the BSS-disentangled IE signal against the standard DTI fitting, Pasternak's, and Collier's free-water elimination (FWE) for subject two.** Comparisons of the FA (b) and MD (d) histograms calculated from the separated IE signals are plotted against the standard DTI, Pasternak's, and Collier's method fit for the short TE measured data. MD (c) and colored FA (a) maps are also included for comparison. We observed a CSF correction effect in the long ΔTE BSS for FA in agreement with Pasternak's FWE. However, both method disagree for MD, where Pasternak's introduces spatial over-regularization. Collier's method did not converge for our single-shell acquisition.

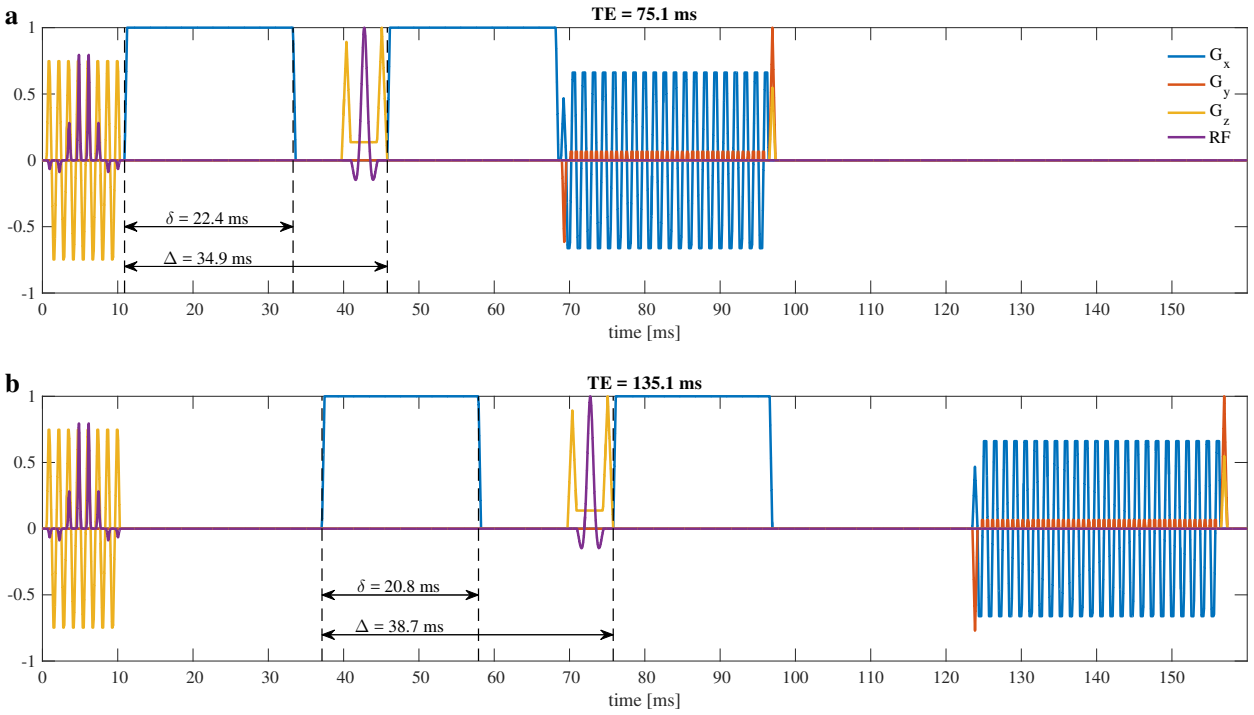

Figure S23: **Pulsed gradient spin echo (PGSE) sequence for the TE values used for the in vivo experiments.**

We show the waveforms measured in our scanner (3.0 T GE MR750w, GE Healthcare, Milwaukee, WI) for b=1000 s/mm^2 and TE equal 75.1 (a) and 135.1 ms (b). The gradient width (δ) and the mixing time (Δ) are 1.6 and 3.8 ms apart respectively. For long TE values the scanner optimizes for maximum gradient amplitude and minimum δ by increasing Δ. These differences in δ and Δ induce dissimilar diffusion sensitization. We show in Figure S24 their effects for IE and CSF Gaussian diffusivities.

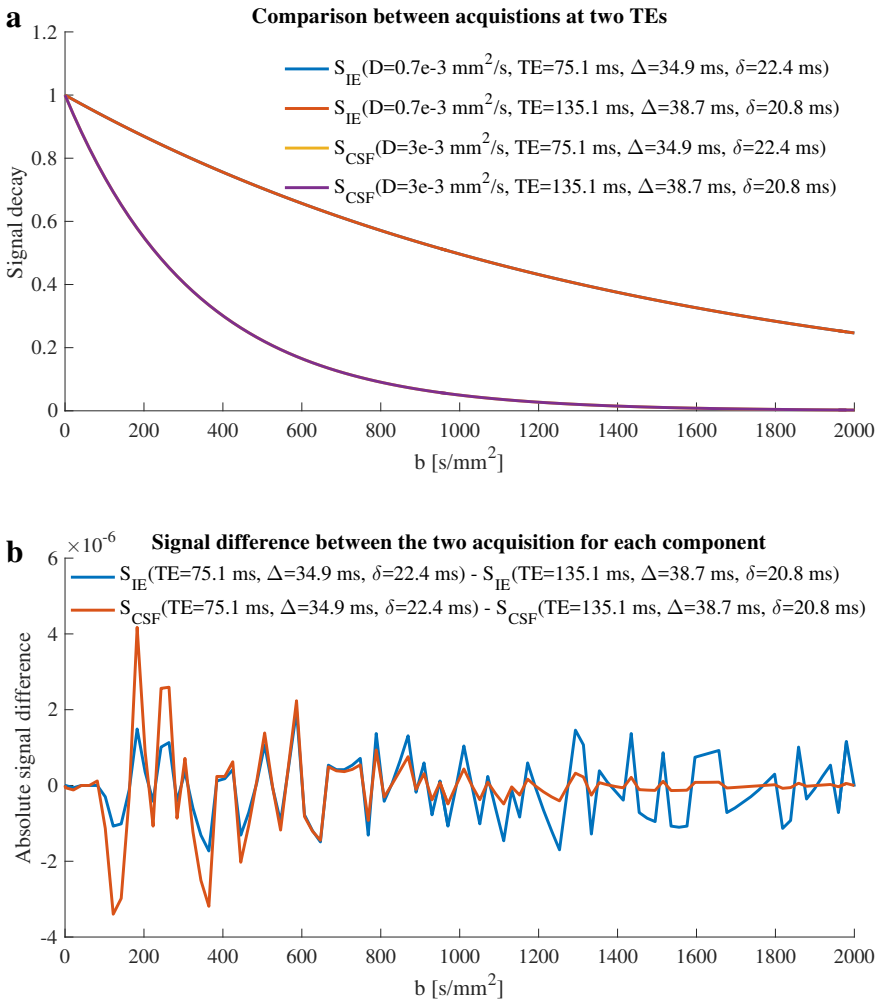

Figure S24: **Normalized simulated signals for IE and CSF for the two combinations of TE, δ, and Δ.**

We ran four Monte-Carlo simulations with Camino (66). IE and CSF diffusivities were modeled as Gaussian processes with values 0.7×10^{-3} and 3×10^{-3} mm^2/s respectively (28). These were measured for the measured PGSE waveforms (a) (See Figure S23). The signal differences (b) were six order of magnitude smaller than the signal. These were due to numerical errors and not to the differences in δ and Δ.